Received: 21 April 2023 | Accepted: 7 September 2023

DOI: 10.1002/suco.202300324

ARTICLE

fib CEB-FIP WILEY

Bond of steel reinforcement based on detailed measurements: Results and interpretations

Enrique Corres | **Aurelio Muttoni**

Ecole Polytechnique Fédérale de Lausanne, School of Architecture Civil and Environmental Engineering, Lausanne, Switzerland

Correspondence
Enrique Corres, Ecole Polytechnique Fédérale de Lausanne, School of Architecture Civil and Environmental Engineering, Lausanne, Switzerland.
Email: enrique.corressojo@epfl.ch

Funding information
Swiss Federal Roads Authority (FEDRO), Grant/Award Number: AGB/2019/017

Abstract

Rebar-to-concrete bond is a fundamental aspect of the behavior of reinforced concrete structures. The characterization of the interface response is challenging due to the complexity of the physical phenomena and the large number of factors involved. Locally, the response is characterized by the bond–slip relationship, which is typically obtained experimentally from pull-out tests with short bonded lengths. The behavior of longer anchorages in structural members differs significantly from short tests as the bond stress distribution is not uniform. In this context, this paper presents the results of a comprehensive research aiming to establish a better relationship between the local bond–slip response from short pull-out tests and the response of medium-length anchorages. The results of an experimental program are presented, including the effect of some parameters commonly found in structural applications, such as casting conditions, clear cover, rib geometry, and rib orientation. A local bond–slip relationship for well-confined conditions is proposed on the basis of the tests performed by the authors and on the examination of a database on short pull-out tests from the literature. Based on this relationship and some mechanical considerations, the local bond–slip relationship for unconfined conditions can satisfactorily be formulated based on crack-width measurements from the concrete surface. This can be useful for the assessment of existing structures and can be seen as a step forward in the development of a consistent mechanical model for bond.

KEYWORDS

anchorage, bond, bond–slip relationship, casting conditions, cover effect, pull-out tests, rib geometry effect, spalling, splitting, structural concrete

1 | INTRODUCTION

The transmission of longitudinal forces between straight reinforcement bars and the surrounding concrete is made possible by the bond forces. Consequently, the rebar-to-concrete bond is a key parameter in the structural behavior of reinforced concrete structures at the serviceability limit state (SLS) as well as at the ultimate limit state (ULS). However, the complexity of the physical phenomena involved in this interaction hinders its characterization.

At a local level, the response is related to the relative displacement between the bar δ_s and the concrete δ_c (slip δ_{sc}, Figure 1a,c), which is inherently associated with the interaction of the rib lugs with the concrete and its

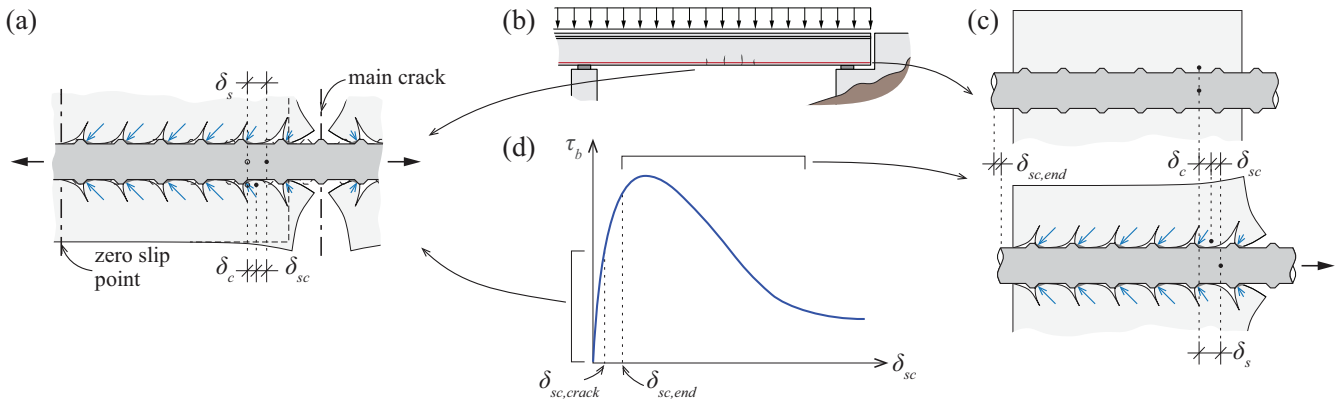

FIGURE 1 Bond in structural members; schematic representation of (a) a cracked region, (b) a reinforced concrete beam, and (c) an end anchorage; and (d) general bond–slip relationship.

internal cracking. For this reason, the interface response is typically characterized by the relationship between the slip and the bond stress (τ_b, Figure 1d), which is often assumed to be uniformly distributed over the nominal surface of the bar.[1] In structural members, the bond behavior of the bar is a consequence of the different conditions along the bonded length (Figure 1b). In a cracked member it is sometimes assumed that the point of the bar halfway between cracks has no slip, due to compatibility, and that the point at the crack slips by approximately half of the crack width. The reality is more complex, the point between cracks can slip due to the crack sequence and different effects cause a variation of the crack width along the cover,[1] as shown in Figure 1a. Nevertheless, bond stresses remain relatively small and have a direct influence on the crack width and the so-called tension stiffening (reduction of steel strains due to activation of concrete in tension between two cracks). In an anchorage or in a lap splice, the bond is necessary to transfer the force in the reinforcement to the concrete or to another bar through the concrete. In these cases, the unloaded end of the bar can slip, leading to the activation of larger bond stresses, particularly at ULS, as illustrated in Figure 1c.

Extensive research on the topic has shown that bond is affected by numerous parameters, including the concrete properties, the bar properties and geometry, the stress state of both materials, the confinement (provided by the concrete cover, by transverse reinforcement, or by transverse pressure), the relative position of the bar with respect to the casting direction, the type of loading and the test conditions amongst others.[1,2] This complexity is reflected in the broad range of local bond–slip relationships that can be found in literature.[3–7]

Current standards account for this complex mechanism and some of the aforementioned parameters in a simplified manner. For instance, in the calculation of the anchorage and lap lengths, constant bond strength is often assumed as in *fib* Model Code 2010[7] (MC2010), Eurocode 2[8] (EC2:2004), or SIA 262:2013.[9] The drafts for the new generation of standards have opted for another approach, providing the bond length directly on the basis of the steel stress to be activated.[10–12] These provisions are based on the expression of *fib* Bulletin 72,[13] where the stress that can be activated in an anchored bar is derived semi-empirically from a statistical study of a large test database. The nonlinearity in the relationship between the steel stress that can be activated and the bond length accounts indirectly for a nonconstant distribution of the bond stresses along the bond length. With respect to the crack width formulations at SLS, the code provisions usually consider a rigid-plastic bond–slip relationship where the bond strength is explicitly or implicitly considered in the calculation of the crack spacing and the tension stiffening effect.[7,8]

MC2010 also provides a local bond–slip relationship for ribbed bars subjected to monotonic loading that accounts for the effect of concrete compressive strength, bar diameter, casting conditions (also called bond conditions), concrete cover, and confinement. Additional expressions are provided to consider the effect of bar yielding, transverse and longitudinal cracking, and other types of loading.[7] The relationship is based on experimental results from pull-out tests in well-confined conditions with short embedment lengths (typically five times the nominal diameter of the bar Ø) and a certain unbonded length at the loaded end of the bar to prevent the development of conical cracks.[14,15] These relationships are based on the work of Eligehausen et al.[3] and adapted on the basis of the expressions from *fib* Bulletin 72 for low and moderate confinement (so-called splitting failures).[13] They are applicable to ribbed bars respecting the bond index or relative rib area (f_R) requirements of

TABLE 1 Main experimental program characteristics and coefficient of variation for the maximum bond stress ($\tau_{b,max}$) and its corresponding slip ($\delta_{sc}(\tau_{b,max})$) of identical tests from the literature.

Reference	Test type	Series	Specimens	Ø (mm)	$l_b/Ø$	CoV $\tau_{b,max}$	CoV $\delta_{sc}(\tau_{b,max})$
Eligehausen et al.[3]	Pull-out	1.1–1.5	2 or 3	25.4	5	1%–12%	2%–14%
Tepfers et al.[50]	Ring test	4	5	16	3	7%	23%
Metelli et al.[16]	Pull-out	13	7	12	5	15%	
		14	7	20	5	18%	
Moccia et al.[38]	Pull-out	BL5D12-S5	3	12	5	7%–10%	8%–18%
		BL5D20-S5	3	20	5	2%–8%	3%–10%

current standards to ensure a good bond performance (EC2:2004 requires a minimum value of 0.056 for bars with a nominal diameter larger than 12 mm[8]). Metelli et al.[16] conducted an experimental program with 151 pull-out tests to evaluate the effect of the bond index, showing that bars with the minimum bond index can reach higher bond strengths and stiffer responses than the MC2010 relationships. Recent studies using detailed measurement techniques have shown the strain gradients generated in the vicinity of the ribs due to the introduction of the bond forces,[17] the nonuniform bond stress distribution and its evolution in tests with short bonded lengths between 2 and 5Ø.[18,19]

The pertinence of the pull-out test has been questioned, as the stress state in the materials and the cover may not be representative of structural applications.[20] Another test commonly used for bond research is the beam-end test, which provides more flexibility for the concrete cover and bonded length.[21] A recent experimental campaign compared the results of pull-out and beam-end tests with a bonded length of 2Ø, observing no influence of the test setup for slip values below 0.1 mm and a 3%–5% increase of the bond strength for pull-out specimens with comparable confinement.[22] It must be noted that being a phenomenon of local nature, the variability observed in experimental results of theoretically identical specimens can be in the range of 1%–18%, as summarized in Table 1.

For typical bonded lengths in structural applications, the assumption of a uniform bond distribution is unrealistic. This was experimentally observed already in the 1950s using bars instrumented with strain gauges placed near their axes with various test setups,[23,24] providing information about the local bond–slip at different positions along the bond length.[4,25] However, the measurement resolution was limited by the minimum spacing between gages.

The improvements in the recent years of fiber optic sensing (FOS) and digital image correlation (DIC) have shown great potential to better understand the bond phenomenon. FOS provides pseudo-continuous strain measurements along the bars with high spatial resolutions and acquisition frequencies. DIC systems allow for detailed measurements of the displacement field over large regions of the specimen's surfaces. Recent works have used this technique to gain a better understanding of the local bond–slip relationship and the distribution along bars in different structural members.[17,19,26]

Several efforts have been made to establish a correlation between the local phenomenon and the bond performance in structural members. Balázs[27] proposed a crack width model based on the integration of the local bond–slip relationship proposed in the *fib* Model Code 1990,[28] assumed to be valid over the bar. This model justifies the variation of the average bond strength for different crack widths. Nevertheless, it ignores the effect of proximity to the crack face, which leads to lower bond forces due to the development of conical cracks at the rib lugs.[15] This effect is often considered by a reduction factor multiplying the local bond stresses with a linear[7] or exponential decrease[29] toward the loaded end of the bar. Furthermore, longitudinal cracking along the bar has been shown to significantly reduce the bond stresses, and several models have been proposed to account for this effect.[5–7,30–32]

The approximations with constant bond stress along the bond length are reasonable and practical for many design purposes. Nevertheless, a better understanding of the underlying mechanisms is required to verify the limits of applicability of current expressions, to develop mechanical models that can more easily be extended to new materials, and to refine the design models. This is necessary to build efficient new structures and to better assess the state of existing ones (e.g., for a more refined fatigue verification accounting for the bar-concrete interaction or to estimate the residual resistance of anchorages affected by longitudinal cracks due to corrosion). Furthermore, local bond–slip relationships are used in finite element models. In this context, the aim of the present research is to investigate the bond behavior in specimens with medium anchorage lengths where conical and longitudinal cracks can develop to establish a better understanding of the effect of visible deteriorations on the

concrete surface on the local bond stresses. The influence of some parameters commonly found in structural applications, such as concrete cover, casting direction, and rib geometry, is considered in an experimental program consisting of 29 pull-out tests instrumented with DIC and FOS. The experimental results show the interaction between the crack development and the local bond stresses that can be activated. On that basis, a local bond–slip model is proposed for well-confined conditions and adjusted based on crack-width measurements to explain the results for low and moderate confinement conditions.

2 | EXPERIMENTAL PROGRAM

An experimental program was conducted in the Structural Concrete Laboratory of the École Polytechnique Fédérale de Lausanne (Switzerland) to investigate the effect of different parameters on the behavior of steel reinforcement bars anchored in concrete and the influence of the cracks visible in the surface of the concrete on the local bond–slip relationship. The results of three tests performed by Moccia et al.[33] (series CM11) are included as well.

2.1 | Series PC01 and PC02

2.1.1 | Specimens

Two series of pull-out tests were conducted using bars with a nominal diameter (Ø) of 20 mm: series PC01 with 4 specimens and an anchorage length (l_b) of 10Ø and series PC02 with 22 specimens and an anchorage length of 15Ø. In all specimens, the bonded length corresponds to the full anchorage length, with the aim of representing realistic anchorage conditions where conical cracks can develop near the loaded end of the bar. The following parameters were investigated in these series:

- Clear concrete cover c: $1Ø \le c \le 5Ø$.
- Casting position: Bars placed horizontally in the formwork were located at the top and bottom position, and bars placed vertically in the formwork were pulled in the same or opposite direction of casting (Figure 2b).
- Rib geometry: Three types of bars with ribs composed of two and four lugs were tested.
- Lug orientation: For bars with ribs composed of two lugs, tests were conducted with the lugs oriented parallelly (//) or perpendicularly (⊥) to the concrete-free surface; the bars with four lugs were placed with the lugs in a 45° disposition with respect to the concrete surface (×), see Figure 2c.

The bars to be tested were embedded in a concrete prism, with one dimension corresponding to the anchorage length and the other being 400 mm. The concrete prisms were reinforced in the longitudinal direction with three 18-mm bars to control cracking during the tests. The spacing between test bars on the same side of the specimen was 800 mm, and their position within opposite sides was shifted by 400 mm. Figure 2a shows the geometry of the specimens and the main investigated parameters of the series. Details about the test parameters of each specimen are provided in Table 2.

2.1.2 | Material properties

All specimens from each series were produced from one batch of normal-strength ready-mixed concrete provided by a local supplier with a maximum aggregate size of 16 mm. The concrete was poured in two layers of approximately 200 mm. The compressive strength f_c of the concrete measured on cylinders (height × diameter = 320 × 160 mm) is indicated in Table 2. The tensile strength measured at 28 days by direct tensile tests with the same type of cylinders was 2.6 MPa for series PC01 and 2.5 MPa for series PC02.

Three types of 20-mm diameter steel bars with rib profiles commonly found nowadays in Switzerland were used in the pull-out tests. The stress-strain diagrams are shown in Figure 3a. The bars display different characteristics:

- Quenched and self-tempered (QST) bars: Hot rolled, QST bars with a well-defined yield plateau. The ribs are composed of two lugs with a nonsymmetrical distribution, see Figure 3b.
- Cold-worked (CW) bars: CW bars with no clear yield plateau (nominal yield strength determined at 0.2% residual strain). The ribs are composed of four lugs disposed symmetrically along the axis of the bar, see Figure 3c.
- Threaded bars for reinforced concrete (TB): steel bars with no clear yield plateau (nominal yield strength determined at 0.2% residual strain). The ribs are composed of two lugs disposed in continuous threads along the axis of the bar, see Figure 3d.

The geometrical characteristics of the bar, including the bond index f_R, the maximum rib height $h_{R,max}$, the transverse rib angle β, the transverse rib flank inclination α_R, and the transverse rib spacing s_R are obtained from a laser scan of the surface of the bars according to their definition.[34] The average rib height $h_{R,avg}$ is calculated by dividing the projected rib area over the nominal bar

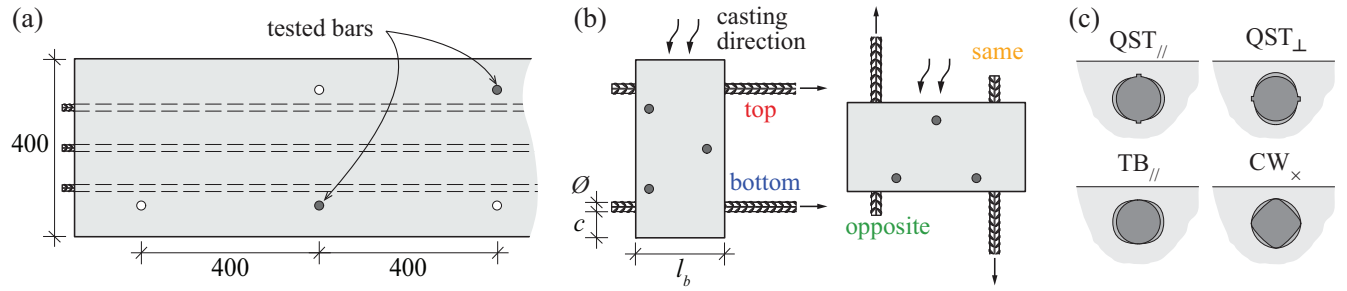

FIGURE 2 Specimen geometry and main investigated parameters of series PC01 and PC02: (a) front elevation of a typical concrete prism containing the test bars; (b) investigated casting positions; and (c) investigated rib geometries and lug orientations (refer to Figure 3 for the used symbols describing the rib geometries).

TABLE 2 Series PC01 and PC02 main parameters and experimental results (for definition of parameters, refer to section Nomenclature).

Specimen	Ø	l_b/Ø	c/Ø	Casting	Bar type	Rib orientation	f_c (MPa)	F_{max} (kN)	σ_{sR} (MPa)	$\tau_{b,max}$ (MPa)	$\tau_{b0.1}$ (MPa)	Failure mode
PC0106	20	10	1	Top	CW	×	39.5	76.3	243	6.1	4.1	S
PC0108	20	10	1	Bottom	CW	×	39.5	87.9	280	7.0	6.4	S
PC0101	20	10	3	Top	CW	×	40.6	93.7	298	7.5	6.6	SPO
PC0103	20	10	3	Bottom	CW	×	39.5	115.5	368	9.2	7.0	SPO
PC0201	20	15	1	Top	QST	//	40.6	96.1	306	5.1	3.4	S
PC0202	20	15	1	Top	QST	⊥	40.5	88.5	282	4.7	3.2	S
PC0203	20	15	1	Bottom	QST	//	40.7	115.6	368	6.1	5.1	S
PC0204	20	15	1	Bottom	QST	⊥	40.7	119.6	381	6.3	5.9	S
PC0205	20	15	3	Top	QST	//	40.9	114.8	365	6.1	4.8	SPO
PC0206	20	15	3	Top	QST	⊥	40.9	125.5	400	6.7	2.4	SPO
PC0207	20	15	3	Bottom	QST	//	41.0	163.5	521	8.7	7.0	SPOy
PC0208	20	15	3	Bottom	QST	⊥	40.9	167.3	533	8.9	7.1	SPOy
PC0209	20	15	5	Top	QST	//	41.1	158.5	504	8.4	5.8	SPOy
PC0210	20	15	5	Top	QST	⊥	41.1	160.5	511	8.5	3.0	SPOy
PC0211	20	15	5	Bottom	QST	//	41.2	>171	>545	>9.1	8.3	–
PC0212	20	15	5	Bottom	QST	⊥	41.2	>175	>557	>9.3	7.1	–
PC0213	20	15	1	Opposite	QST	//	41.3	106.0	337	5.6	5.6	S
PC0214	20	15	3	Opposite	QST	//	41.4	157.1	500	8.3	6.6	SPO
PC0215	20	15	5	Opposite	QST	//	41.4	163.0	519	8.6	8.1	SPOy
PC0216	20	15	1	Same	QST	//	41.5	107.8	343	5.7	5.1	S
PC0217	20	15	3	Same	QST	//	41.5	133.9	426	7.1	4.9	SPO
PC0218	20	15	5	Same	QST	//	41.5	163.7	521	8.7	7.2	SPOy
PC0220	20	15	5	Top	CW	×	41.3	133.5	425	7.1	4.6	SPO
PC0221	20	15	5	Bottom	CW	×	41.3	149.8	477	7.9	6.7	SPO
PC0222	20	15	5	Top	TB	//	41.2	140.1	446	7.4	5.9	SPO
PC0223	20	15	5	Bottom	TB	//	41.3	176.0	560	9.3	8.0	SPO

Note: $\sigma_{sR} = F_{max}/(\pi \times Ø^2/4)$. $\tau_{b,max} = F_{max}/(\pi \times l_b \times Ø)$.
Abbreviations: S, spalling before yielding of the reinforcement; SPO, splitting induced pull-out before yielding; SPOy, splitting induced pull-out after yielding; –, test stopped after extensive yielding without anchorage failure.

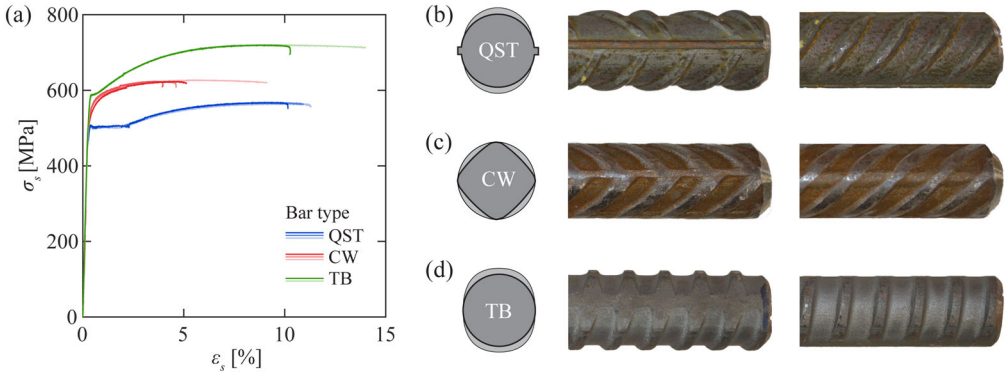

FIGURE 3 Bar characteristics: (a) stress–strain curves; and cross-section and pictures of (b) QST bars, (c) CW bars, and (d) TB bars.

TABLE 3 Bar mechanical and geometrical properties (for definition of parameters, refer to section Nomenclature).

Type	Ø (mm)	f_y (MPa)	f_t (MPa)	Lugs	f_R	$h_{R,avg}$ (mm)	$h_{R,max}$ (mm)	s_R (mm)	c_{clear} (mm)	β (°)	α_R (°)
QST	20	504	567	2	0.075	0.94	1.46	12.63	8.17	52.6	33.9
CW	20	558	625	4	0.079	0.94	1.42	11.91	6.83	42.4	37.5
TB	20	587	726	2	0.089	0.88	1.43	9.90	6.38	80	46.8

perimeter. The clear spacing between ribs c_{clear} is considered as the spacing between consecutive rib flanks at mid-height of the ribs based on the laser scans. The main properties of the bars are summarized in Table 3.

2.1.3 | Test setup and test development

All specimens were tested with the bar oriented in the vertical direction, as illustrated in Figure 4a,b. The bar was clamped with a steel wedge, and the pull-out force was exerted through a hinge to minimize bending in the bar. The reaction on the concrete specimens was applied through a steel frame to minimize the influence on the development of concrete cone breakouts. The frame was composed of two UPN 120 profiles, and the frame legs were SHS 50 × 50 × 5 mm with 70 × 70 × 20 mm steel plates welded at the extremities. In each test, the frame was aligned with the axis of the bar. The frame was hinged at the position of the bar to minimize the bending moment in the concrete prism in the bar region. Two 16-mm threaded bars were used to counterbalance the applied force. The tests were conducted by applying the load at a constant loading rate, reaching the maximum load in 4–5 min. After the maximum force was reached, the test continued at a constant displacement rate to capture the post-peak response.

2.1.4 | Measurements

The force applied to the bar, and the reactions on the threaded bars were measured using load cells. The slip between the bar and the concrete at the unloaded end was measured with two LVDTs. The concrete surface parallel to the bar was tracked with DIC (see "DIC area" in Figure 4a) using a pair of cameras SVS EVO4070 with a resolution of 4.2 Mpix. The correlation was done using the VIC-3D software,[35] with a pixel size of 235 μm for series PC01 and 255 μm for series PC02. The displacement error was 1/75 pixels for in-plane displacements and 1/30 for out-of-plane displacements. The data acquisition frequency was 1 Hz.

The reinforcement bars were instrumented using a single fiber optic installed along two opposite sides of the specimen, as illustrated in Figure 4b. Polyimide-coated fibers with a diameter of 125 μm were used (Figure 4d). The fibers were placed in a groove 1-mm wide and 2-mm deep that runs along the opposite faces of the bars. The position of the grooves was chosen to keep the fibers in a plane perpendicular to the concrete surface, independently of the rib orientation, see Figure 4c. The strains were measured using Optical Distributed Sensor Interrogator ODiSI-6100 by Luna Innovations with a strain measurement range of ±12,000 με and a measurement accuracy of ±25 με.[36] The spatial resolution of the strain measurements was 0.65 mm, and the acquisition frequency varied between 40 and 62.5 Hz. It must be noted that for QST bars with a clear yield plateau, the yielding of the bar leads to strains larger than the measurement range and, therefore, to the loss of the fiber measurements.

2.2 | Series CM11

Specimens of the pull-out test series CM11 conducted by Moccia et al.[33] had the same geometry as specimens from

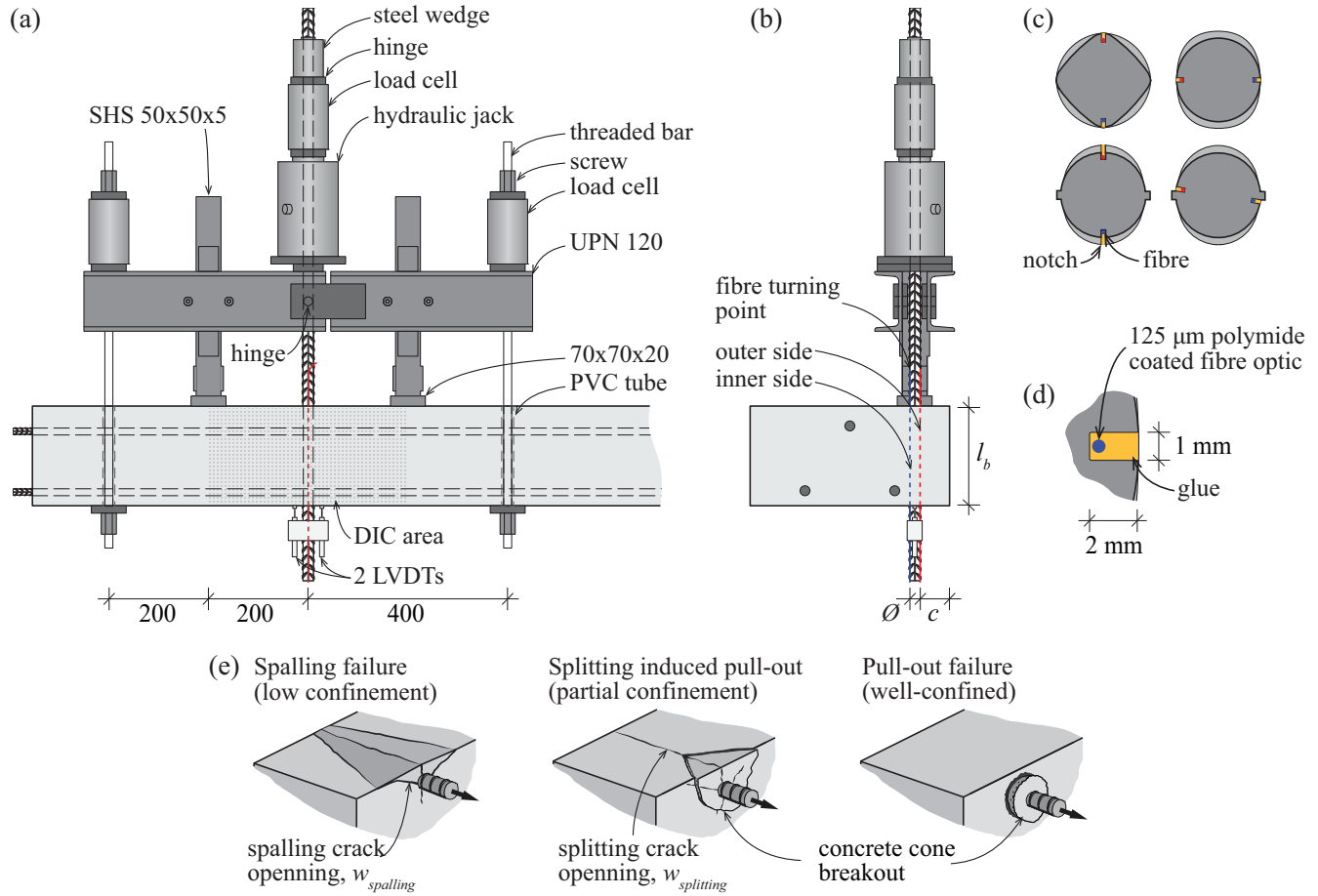

FIGURE 4 Test setup, measurement systems and typical failure modes in the pull-out tests: (a) front and (b) side elevation of the test setup; (c) position of fiber optic sensors in the different types of bars; (d) optical fiber detail; and (e) typical failure modes in pull-out tests.

TABLE 4 Series CM11 main parameters and experimental results (for definition of parameters, refer to section Nomenclature).

Specimen	Ø	l_b/Ø	c/Ø	Casting	Bar type	Rib orientation	f_c (MPa)	F_{max} (kN)	σ_{sR} (MPa)	$\tau_{b,max}$ (MPa)	$\tau_{b0.1}$ (MPa)	Failure mode
CM1120	20	10	1	Top	QST	⊥	42.3	64.0	204	5.1	2.3	S
CM1128	20	10	1	Bottom	QST	⊥	42.3	70.8	225	5.6	5.2	S
CM1124	20	10	3	Top	QST	⊥	42.3	94.7	302	7.5	5.4	SPO

Note: $\sigma_{sR} = F_{max}/(\pi \times Ø^2/4)$. $\tau_{b,max} = F_{max}/(\pi \times l_b \times Ø)$.
Abbreviations: S, spalling before yielding of the reinforcement; SPO, splitting induced pull-out before yielding.

series PC01. The steel bars with a nominal diameter of 20 mm were embeded in a concrete prism 200 × 400 mm, corresponding to a bonded length of 10Ø. The evaluated parameters in the test series were the concrete cover and the casting conditions. The main properties of the specimens are summarized in Table 4. The average concrete strength at the time of the tests was 42.3 MPa. The hot-rolled QST steel bars had a distinct yielding plateau, an average yield strength of 521 MPa, and a tensile strength of 620 MPa. The ribs were composed of two lugs with a nonsymmetric disposition and a bond index $f_R = 0.072$. The tests have been conducted in a similar manner as for series PC (more details can be found in Moccia et al.[33]).

2.3 | Data postprocessing

The strain measurements along the bonded length show local variations due to the variable cross-section of ribbed bars, the potential variable material properties within the

cross-section, the noise in the measurement system, and the transmission of bond forces at the ribs.[17,37] These local strain oscillations have to be removed to calculate nominal bond stresses. A moving average filter over a length corresponding to three times the rib spacing (around two bar diameters) was applied to the raw strain measurements for the analysis of the test results. This distance is similar to the disturbed length observed in pull-out tests of bars with one and two ribs performed by Cantone et al.[17] For the measurement of the strain due to shrinkage, a distance of ten rib spacings was used. The average strain was computed from the smoothed measurements of the two fibers. The stresses were calculated considering the stress–strain relationship obtained from tensile tests of grooved bare bars with fibers. The pertinence of this assumption was verified with the average strain measurements over a length of four rib spacings from the loaded end of the bar outside the concrete (Figure 4a). Bond stresses are derived from the smoothed stress profiles using Equation (1), which can be obtained from the equilibrium of a differential bar element.

$$\frac{d\sigma_s}{dx} = \frac{4\tau_b}{\emptyset}. \quad (1)$$

2.4 | Failure modes

The typical failure modes in pull-out tests and the definitions used in this paper are illustrated in Figure 4e. Regardless of the test conditions, all specimens developed a splitting crack (parallel to the bar and approximately perpendicular to the concrete surface). Specimens with a cover of 1Ø failed by spalling of the concrete cover (failure mode "S" in Tables 2 and 4) with the propagation of two longitudinal cracks along the bar with a small angle with respect to the concrete surface. Specimens with a cover of 3 and 5Ø displayed a splitting-induced pull-out failure ("SPO"). Some bars with an anchorage length of 15Ø yielded ("SPOy"), and two tests with QST bars at the bottom of the formwork (good casting conditions) were stopped when the stresses approached the tensile strength of the bar. Detailed crack patterns for all specimens are provided in Appendix A.

3 | EXPERIMENTAL RESULTS

3.1 | Shrinkage

Strain measurements from the fiber optic sensors were recorded 6 h after the casting (Day 0 measurements) and before testing. The measurements from the bar outside the concrete were used to remove the effect of temperature variation, assuming a uniform temperature distribution along the bar. Figure 5a,b show the results for specimens PC0206 and 08, including the raw strain measurements (ε_s) from the external (closest to the concrete surface, red curves) and internal fibers (located in the opposite face of the bar, blue curves), the smoothed average stress (σ_s) and the bond stress. In specimen PC0206 (poor casting conditions), the signal presents large strain variations reaching strains over 1.5‰ for the external fiber and regular low amplitude variations for the internal fiber. In specimen PC0208 (good casting conditions), both signals show strain variations reaching approximately 1‰, similar to the measurements by Lemcherreq et al.[19] The difference can be explained by the presence of plastic settlement voids under bar PC0206, which limit the capacity of the concrete to transfer forces to the bar.[38] The bar in good casting conditions is surrounded by concrete on all sides, thus causing a similar strain profile on both sides of the bar. Similar trends could be observed in other specimens, with the ribs oriented perpendicularly to the concrete surface.

The fiber measurements were smoothed using a moving average filter over a distance of 10 rib spacings (126 mm). The resulting stress profiles are coherent with those found in literature.[19,39] The bar in poor casting conditions displays a minimum stress of −5.6 MPa and an average bond stress of 0.2 MPa (average value at each side of the maximum steel stress, see Figure 5a) with maximum local values close to 0.5 MPa. For the bar in poor casting conditions, the minimum steel stress was −10.9 MPa with an average bond stress of 0.4 MPa, see Figure 5b. The results indicate that smaller shrinkage axial and bond stresses are induced in the bar in poor casting conditions due to plastic settlement voids. Nevertheless, these results must be considered with care as the peak raw strain measurements are two orders of magnitude larger than the shrinkage strains. Consequently, the results are highly dependent on the smoothing. Further tests are required to confirm these findings.

3.2 | Anchorage resistance

The anchorage resistance expressed in terms of the maximum stress activated in the bar (σ_{sR}) is represented as a function of the anchorage length in Figure 6a–c. The experimental results are compared with the tensile stress that can be developed in the anchorage according to the expression for mean values proposed in the Background Document for the final draft of Eurocode 2 (BD FprEC2:2023).[11,12] In all specimens, the

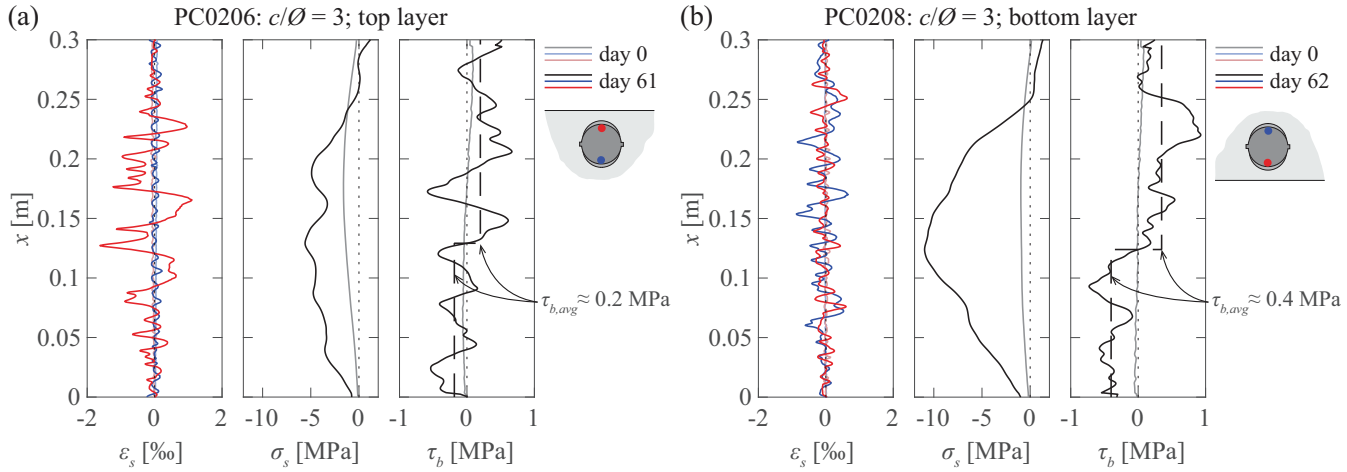

FIGURE 5 Shrinkage-induced effects: distribution along the bonded length of raw strain measurements, axial stresses and bond stresses in the bars for specimens (a) PC0206 and (b) PC0208 (red and blue colors refer to each fiber optic sensor, see sketch, black and gray curves refer to the mean values).

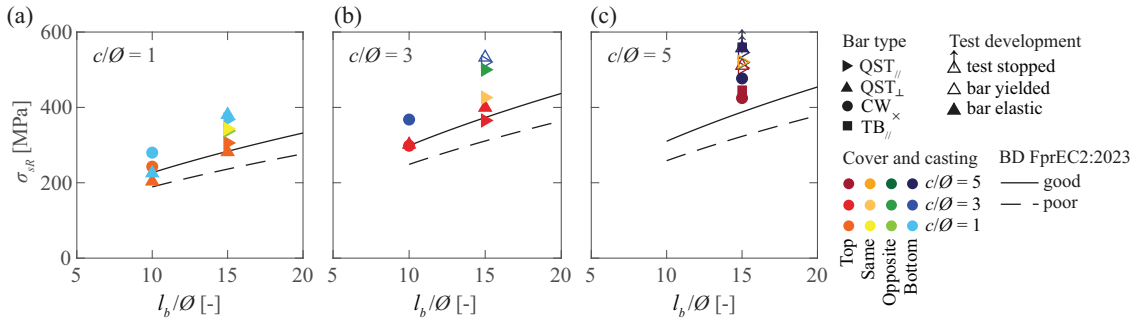

FIGURE 6 Anchorage resistance as a function of the anchorage length for specimens with covers of (a) 1Ø; (b) 3Ø; and (c) 5Ø.

experimental anchorage resistance was larger than the proposed values.

3.3 | Effect of concrete cover and casting conditions

Figure 7a shows the average bond stress over the anchorage length ($\tau_{b,avg}$) as a function of the unloaded end slip ($\delta_{sc,end}$) for specimens with an anchorage length of 15Ø in all the considered casting conditions. The maximum anchorage resistance is reached for good casting conditions (blue), followed by the bars loaded in the opposite direction of casting (green), then by the bars loaded in the casting direction (yellow), and finally, the bars in poor casting conditions (red). Specimens with a cover of 1Ø present a relatively brittle failure with a sudden drop in the force and the consequent lack of experimental data (dotted lines). The influence of the concrete cover and the casting position on the maximum stress activated in the bar is shown in Figure 7b. This difference is caused by the cracks and the voids under the bars due to the plastic settlement of the fresh concrete and the higher porosity of the concrete under the bars.[38,40–42] The effect of the confinement and casting position on the anchorage length is included in current standards; however, its effect on cracking at SLS is not.[7,8] Figure 7c presents the average bond stress corresponding to a slip at the unloaded end of 0.1 mm ($\tau_{b0.1}$) for the considered covers. Significant variations can be obserbed due to the other parameters; however, the linear regression (dashed line) shows an increasing trend for all casting conditions. Therefore, the effect of confinement and casting conditions can be relevant for serviceability verifications. Pérez Caldentey et al.[43] recently proposed an empirical factor for the crack spacing formulation based on the experimental results of four-point bending tests to account for the effect of casting conditions and the effect of cover in poor casting conditions. The results in Figure 7c confirm that the cover can influence the bond stresses at SLS in

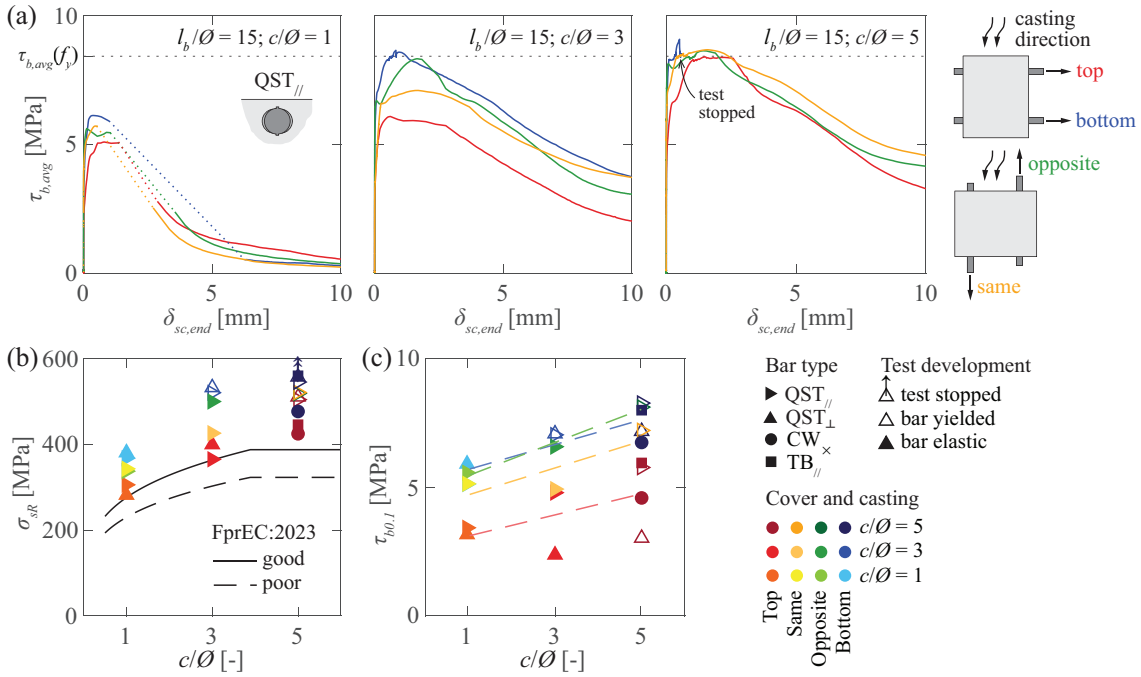

FIGURE 7 Effect of concrete cover and casting conditions: (a) average bond stress–slip relationships for specimens with covers of 1Ø (PC0201, 03, 13, and 16), 3Ø (PC0205, 07, 14, and 17), and 5Ø (PC0209, 11, 15, and 18); (b) anchorage resistance as a function of concrete cover; and (c) average bond stress corresponding to a slip at the unloaded end of 0.1 mm as a function of concrete cover.

all casting conditions. The new generation of standards includes the effect of casting conditions on the crack width formulation.[11]

Figure 8 shows the detailed measurements obtained with DIC and FOS along the anchorage length for specimens PC0201, 05, and 09 with QST$_{//}$ bars in poor casting conditions. For each specimen, the crack opening at the maximum load (F_{max}) is represented in red, and the cracks developed during the post-peak phase are shown in gray in Figure 8a,c,e. This information was extracted from the DIC data using the Automatic Crack Detection and Measurement software.[44] Figure 8b,d,f displays the distribution of raw (light gray curves) and smoothed strains ε_s (red, purple, and dark gray curves), smoothed axial stress σ_s, bond stress τ_b, steel δ_s (dotted curves), and concrete displacements δ_c (dashed curves), relative slip δ_{sc} (solid curves), and crack width w for different load levels. The concrete displacement is calculated from the displacement field on the concrete surface measured with DIC. The bar displacement is calculated by adding the slip at the unloaded end, measured with the LVDTs and the integrated strains along the bar. The relative slip is the difference between these two values. The opening of the spalling crack $w_{spalling}$ (solid curves) is assumed to be equal to the out-of-plane displacement of the concrete cover along the bar axis. The opening of the splitting crack $w_{splitting}$ (dashed curves) is measured using the DIC displacements from the concrete surface (for the definition of splitting and spalling cracks used in this paper, see Figure 4e).

For all specimens, the splitting crack appeared first at the loaded end of the bar and propagated toward the unloaded end. Typically, as the load increased, one or more cracks with a "V" shape developed on the concrete surface along the length of the specimen. These cracks probably correspond to the intersection of conical cracks originating at the ribs[15] with the concrete surface. The development of these cracks can also be observed in the stepped distribution of concrete displacements. Near the loaded end of the bar, the propagation of these cracks caused the breakout of a conical concrete block (dark gray area in Figure 8c,e), causing large displacements and a reduction of the bond stresses. Specimen PC0201 failed by spalling of the cover, the spalled region is indicated with a dark gray hatch in Figure 8a.

The axial steel stress distribution shows that for small load levels, larger bond stresses are activated at the loaded end of the bar. As the load increases, the distribution flattens near the loaded end, indicating lower bond stresses in that region. A redistribution of the bond stresses occurs, and larger bond stresses are activated near the unloaded end, as observed by other authors.[23] After the maximum load is reached, the concrete cone detachment causes bond stresses to vanish within the corresponding length, as can be clearly observed in Figure 8d. In specimen PC0209, whose reinforcement yielded at around

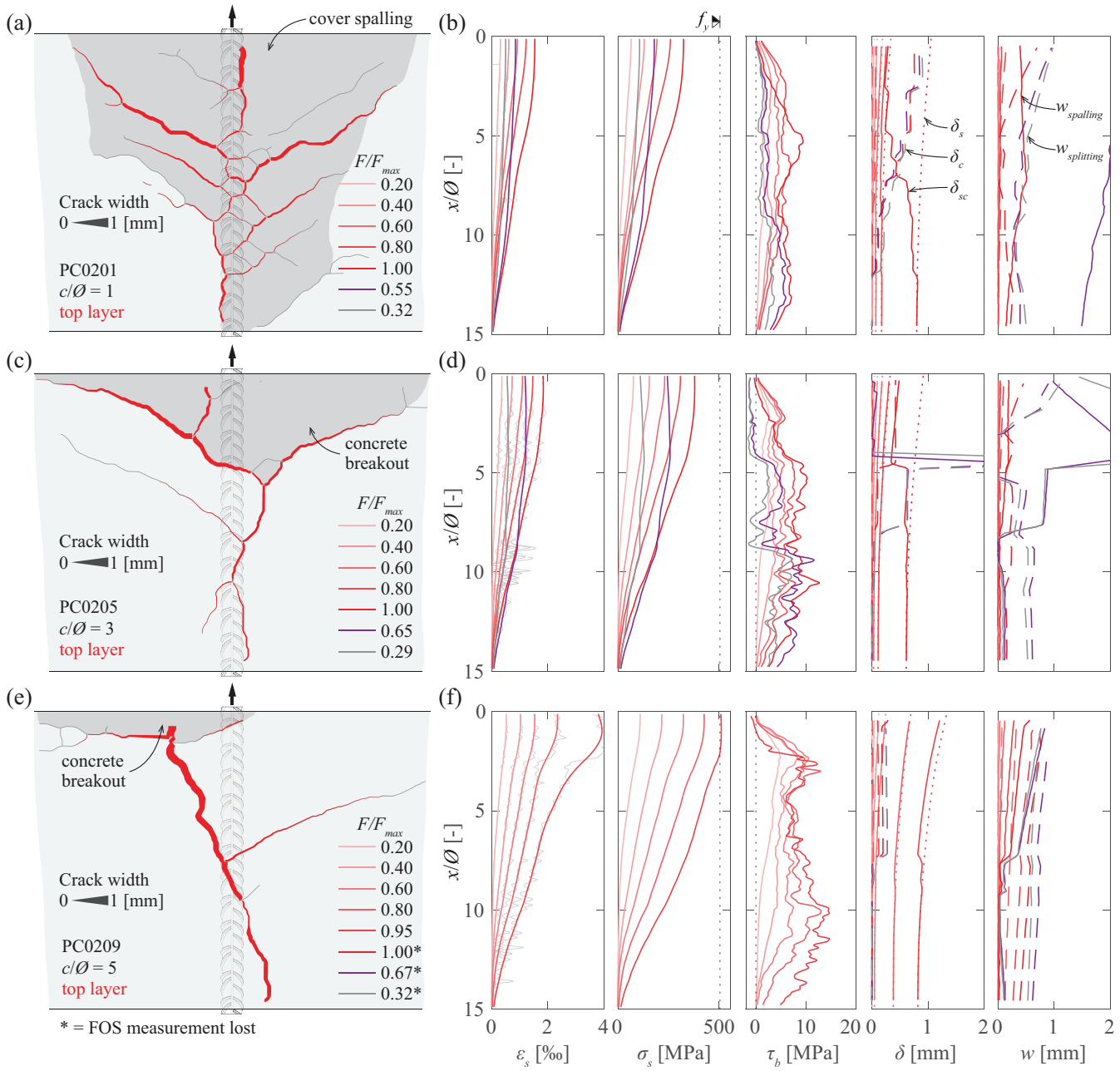

FIGURE 8 Pull-out test detailed measurements: crack pattern and distribution along the anchorage length of axial steel strains, axial steel stresses, bond stresses, slip and crack widths for specimens (a, b) PC0201, (c, d) PC0205, and (e, f) PC0209.

95% of the anchorage capacity, the length of the concrete cone breakout along the bar is similar to the region where yielding was detected (Figure 8f).

The slip plots indicate that the displacement of the concrete can be neglected until the propagation of the conical cracks reaches the concrete surface. The crack opening plots show that the spalling crack width reaches considerably larger values for the bars with a cover of 1Ø. For specimens with larger covers, the splitting crack widths tend to be larger. An interaction between the concrete cone breakout and the splitting and spalling cracks is observed. Within the region affected by conical cracks, larger spalling crack widths occur due to the displacement of the concrete cover. Concerning the splitting crack, as the bar slides, the partially detached concrete blocks composing the cone are pulled. This causes their rotation in opposite directions in the plane of the concrete surface, reducing the splitting crack width near the intersection of the two cracks. Similar crack patterns and stress distributions were observed in other specimens. The results for all tested specimens can be found in Appendix A.

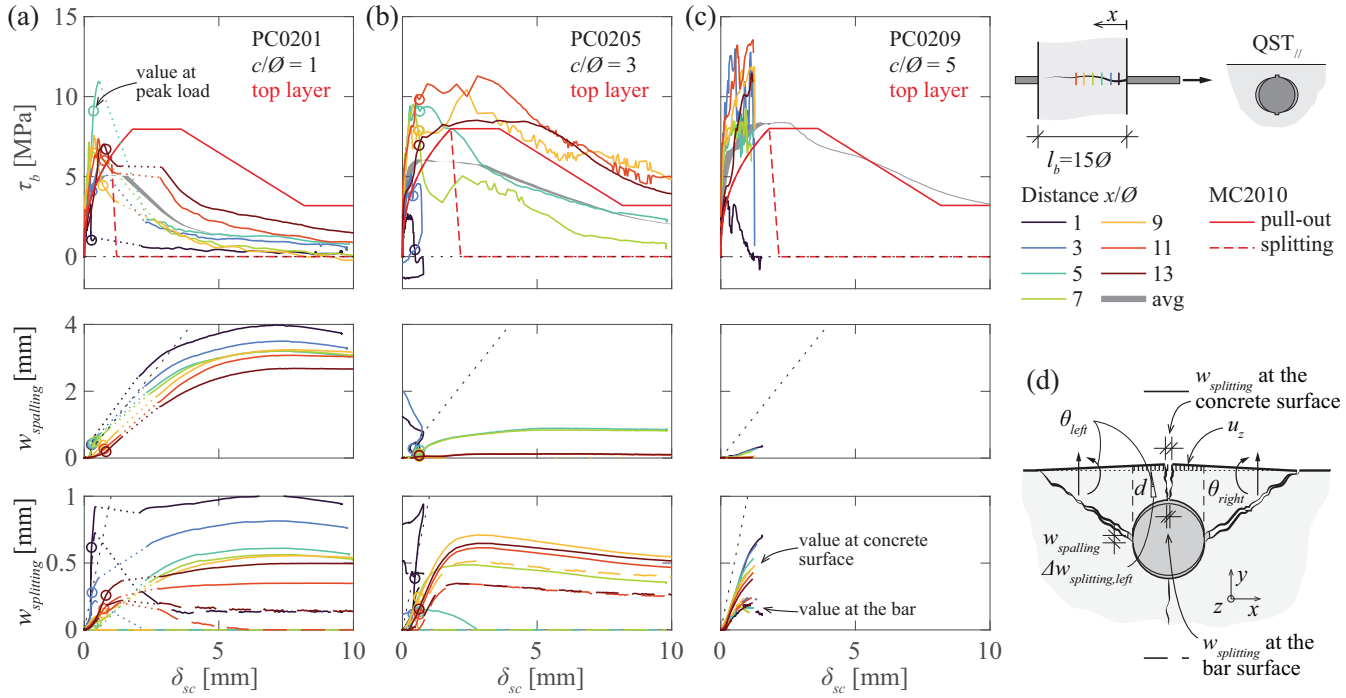

FIGURE 9 Local measurements along the bonded length: local bond–slip, spalling crack opening-slip and splitting crack opening-slip relationships for specimens (a) PC0201, (b) PC0205, and (c) PC0209; and (d) schematic representation of the crack development mechanism.

More detailed information about the local response at various positions along the bar can be obtained from the measurements presented in Figure 8 by plotting the different values as a function of the local slip. The local bond stress–slip distribution and the evolution of the crack widths at different locations are illustrated in Figure 9. The average bond stress as a function of the unloaded and loaded end slips (gray hatch) and the MC2010 local bond–slip relationship (red curves) are represented for comparison. As it can be observed in Figure 9a,b, the average response for specimens with a cover of 1 and 3Ø displays a lower peak bond strength than the MC2010 provisions, which is logical as the MC2010 expressions were calibrated with short pull-out tests with a more uniform bond stress distribution. The local bond stress measurements display similar peak values or even higher for the points not affected by the cone breakout. The local measurements display a less brittle post-peak response than the corresponding relationship according to MC2010 (unconfined splitting failure). This is also probably related to the longer bonded length and the stress redistribution capacity. For the specimen with a cover of 5Ø (Figure 9c), the average response reaches a peak stress close to the MC2010 provision with higher local bond stresses. Points outside the concrete cone breakout display a fairly uniform behavior. Within the breakout region, the local bond stresses reach lower values and have a more brittle response. The response does not seem to correspond to a uniform reduction of the bond stresses as proposed by MC2010, but rather a similar ascending branch with different maximum bond stresses and post-peak responses.[3,45] In all specimens, the measured response displays higher stiffness in the ascending branch than the MC2010 expressions. These results agree with other recent studies using pull-out tests,[16] beam-end tests,[18] and concrete ties.[26]

It must be noted that the crack patterns represented in Figure 8 correspond to the measurements on the concrete surface. The activation of bond forces is directly related to the internal cracking of the concrete around the bar, which can differ from the measurements on the concrete surface. The spalling of the cover causes the rotation of the concrete segments delimited by the splitting and the spalling cracks in a plane perpendicular to the bar, as illustrated in Figure 9d. This rotation increases the crack with the splitting crack on the concrete surface and reduces it at the bar surface. The variation of the crack opening can be estimated by multiplying the rotation at both sides of the crack by the cover. Therefore, the estimated crack width at the bar can be obtained by subtracting the estimated variation from the measurement on the visible concrete face. The pertinence of this estimation was verified and compared with DIC measurements on the surface perpendicular to the bar on the loaded end.[46] The estimated splitting crack

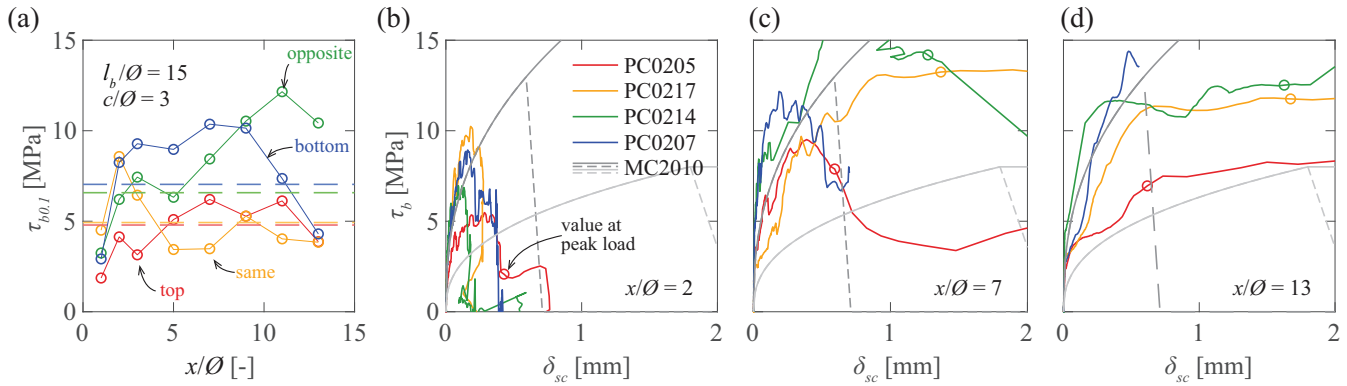

FIGURE 10 Effect of casting position for specimens PC0205, 07, 14, and 17: (a) local bond stress corresponding to a local slip of 0.1 mm along the anchorage length; and local bond–slip relationships at (b) $x/Ø = 2$, (c) $x/Ø = 7$, and (d) $x/Ø = 13$.

width at the bar is shown with dashed lines in Figure 9a–c.

The crack width plots for specimen PC0201 show large spalling crack openings reaching values close to two times the maximum rib height. As the out-of-plane displacements of the cover take place, the width of the splitting crack at the bar is reduced (Figure 9a). Specimens with larger covers show smaller spalling openings, particularly for points outside the cone breakout. Specimen PC0205 shows the largest splitting crack widths at the bar surface (close to 0.5 mm) that remain stable during the post-peak phase, see Figure 9b. The specimen with a cover of 5Ø shows the smallest crack openings, see Figure 9c.

Figure 10a shows the local bond stress corresponding to a local slip of 0.1 mm ($\tau_{b0.1}$) along the anchorage length for specimens with a cover of 3Ø in different casting conditions. The average value for each specimen is represented with a dashed line. The points closer to the loaded end ($x = 0$), which are affected by the concrete cone breakout, typically display lower secant stiffness, with the exception of the bar loaded along the casting direction (yellow curve), which shows a similar stiffness along most of the bonded length and even higher values near the loaded end. In this case, the loaded end is close to the bottom of the formwork (good casting conditions). Outside the cone breakout region, the specimen in the bottom of the formwork (blue curve) and the specimen loaded against the casting direction (green curve) show similar secant stiffnesses larger than for the other conditions. The local response of the specimen at the top of the formwork (poor casting conditions, red curve) is slightly stiffer than the specimen loaded along the casting direction. This seems reasonable because for the bar at the top of the formwork, the voids caused by the plastic settlement of concrete will be located under the bar; whereas for the vertical bar, they will appear under the ribs along the full perimeter of the bar. Nevertheless, the average response yields similar values as the voids will get smaller in the regions close to the bottom of the reinforcement. The difference between these two conditions can differ depending on the distance to the bottom of the formwork.[38]

The local bond–slip responses for the four considered casting conditions at three locations are shown in Figure 10b,c. The results at a distance of 2Ø from the loaded are within the concrete cone breakout and show a brittle response (Figure 10b). The results at 7 and 13Ø from the loaded end reach larger bond stresses and have a less brittle softening response (Figure 10c,d). At each location, the experimental curves show similar behaviors for the different conditions besides the differences in stiffness and peak values. In all cases, the responses are stiffer than the MC2010 relationships.

3.4 | Rib orientation

The measured average bond stresses as a function of the unloaded end slip for specimens with an anchorage length of 15Ø and different concrete covers are illustrated in Figure 11a. The QST bars were placed with two orientations: bars with the ribs oriented parallel to the concrete surface ($QST_{//}$, solid curves) and bars with the ribs oriented perpendicularly to the surface ($QST_{\perp}$, dashed curves). The same general response and failure mode is observed independently of the rib orientation for good (blue curves) and poor casting conditions (red curves). Figure 11b shows the influence of the rib orientation on the maximum stress activated in the bar. The results for specimens in good casting conditions show little influence of the rib orientation. For specimens in poor casting

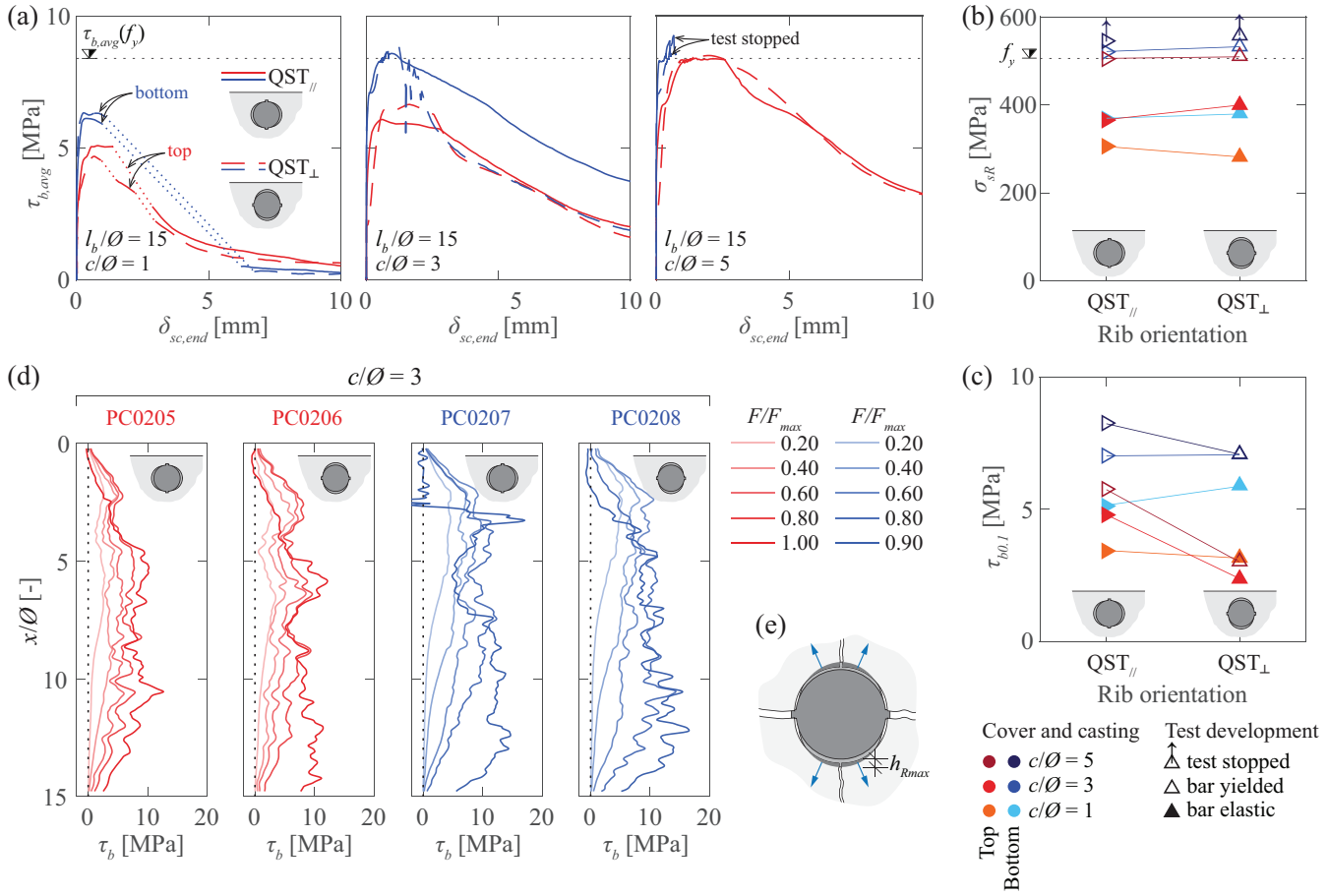

FIGURE 11 Effect of rib orientation: (a) average bond stress–slip relationships for specimens with covers of 1Ø (PC0201 to 04), 3Ø (PC0205 to 08), and 5Ø (PC0209 to 12); (b) anchorage resistance as a function of the rib orientation; (c) average bond stress corresponding to a slip at the unloaded end of 0.1 mm as a function of the rib orientation; (d) local bond stress distribution along the anchorage length for specimens with a cover of 3Ø (PC0205 to 08); and (e) schematic representation of the rib orientation effect.

conditions with a cover of 1Ø (spalling failure), the QST$_{//}$ specimen reached an anchorage resistance 9% larger than the QST$_{\perp}$. For specimens in poor casting conditions with covers of 3 and 5Ø, the anchorage resistance for QST$_{//}$ bars is, on average, 5% lower. Figure 11c shows that the $\tau_{b0.1}$ is, on average, 67% lower for QST$_{\perp}$ specimens in poor casting conditions. The response in good casting conditions shows no difference on average (values of ±15%). This can be explained by the presence of plastic settlement voids and the porous concrete layer that, in the case of perpendicular orientation, directly affect the rib placed toward the bottom of the formwork. For specimens with ribs oriented parallelly to the concrete, only a lower portion of the lugs is affected by the voids. This effect is not present in bars in good casting conditions, which justifies the lack of uniform tendency and values within typical bond test scatter.

Figure 11d illustrates the bond stress distribution along the bar for five load levels for specimens with covers of 3Ø. The results show that for loads close to 20% of the anchorage resistance, bars in poor casting conditions activate lower bond stresses but over a longer portion of the bar, particularly for the QST$_{\perp}$ bar. This is in good agreement with the differences in stiffness (Figure 11c) and can indicate a higher redistribution capacity when the bond–slip relationship is less stiff. Moreover, it can be observed that higher bond stresses are activated near the unloaded end in specimen PC0206, which explains the higher anchorage resistance. The difference in the activation for low load levels can also be observed for specimens with covers of 1 and 5Ø (see Appendix A).

The results seem coherent with the fact that bars with the ribs oriented perpendicularly to the concrete surface will develop a larger component of bursting forces, whereas if the rib lugs are oriented parallelly, there will be a larger component of splitting forces (Figure 11e). Consequently, specimens with a failure mode governed

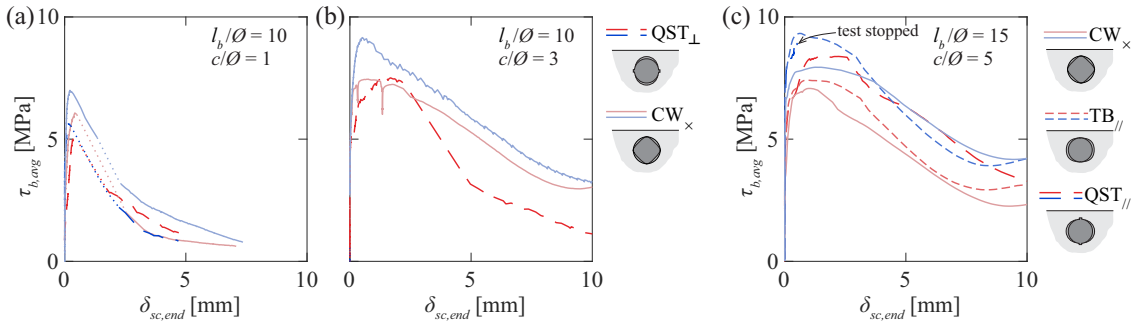

FIGURE 12 Effect of rib geometry: average bond stress–slip relationships for specimens with covers of (a) 1Ø (CM1120, 28, PC0106 and 08), (b) 3Ø (CM1124, PC0101 and 03), and (c) 5Ø (PC0209, 11, 20, 21, 22 and 23).

by spalling (low confinement) can have a lower anchorage resistance if the ribs are placed perpendicularly to the concrete surface. In good casting conditions, the sudden crack development limits the influence of this effect.

Cairns et al.[47] reported that there is a high probability that rib orientation influences the bond strength based on an analytical formulation and an experimental program with lap-splices that favored splitting failure. Koschemann et al.[22] conducted an experimental campaign with beam-end tests with bond lengths of 2Ø investigating the effect of rib orientation on bars with a nominal diameter of 16 mm and rib pattern similar to the QST bars in this publication. The lowest anchorage resistance (around 5%) was observed for specimens with ribs oriented parallel to the concrete surface and the lugs leading to compression struts toward the concrete surface. The experimental results presented in this paper indicate that, for specimens with pull-out or splitting-induced pull-out failures, the influence of the rib orientation is larger in the redistribution of bond stresses than in the crack development. Recent studies on lap-splices[48] and anchorages[49] have shown that local bond–slip relationships with lower peak values and stiffness can lead to higher strengths in poor conditions for long anchorage lengths.

It must be noted that the difference in anchorage resistance due to the rib orientation reported in this study and in the literature lies within the typical scatter observed in bond tests. However, the differences in the secant stiffness for small slip values are significant and indicate that the effect of rib orientation is potentially relevant for SLS conditions.

3.5 | Rib geometry

Figure 12a presents the average bond stress as a function of the unloaded end slip for specimens with an anchorage length of 10Ø and a cover of 1Ø. The results indicate that the anchorage resistance of the QST$_\perp$ bars is lower than for CW bars: 19% for good (blue curves) and 16% for poor casting conditions (red curves). The stiffness follows the same trend, being lower for QST$_\perp$ specimens: 18% for good and 44% for poor casting conditions. This could be explained by the difference in orientation, given the similar geometrical characteristics of these bars. CW bars were placed with the lugs in a 45° disposition with respect to the direction of the concrete surface, therefore generating a lower bursting force component and being less susceptible to the effect of plastic settlement voids. The results for specimens with a cover of 3Ø in poor casting conditions show similar peak bond stresses and lower secant stiffness, see Figure 12b.

Figure 12c shows the average bond stress as a function of the unloaded end slip for specimens with an anchorage length of 15Ø and a cover of 5Ø. For good and poor casting conditions, the QST bars developed the largest anchorage resistance (around 19% higher in poor casting conditions), followed by the TB bars (5% and 17% higher in poor and good casting conditions, respectively) and the CW bars. The difference in the bond indices of the bars does not correlate with the results, as the bar with the lowest bond index (QST) activates the highest bond stresses. In well-confined conditions, the pull-out failure occurs by shearing off the concrete keys between the ribs, and increasing the rib spacing leads to larger bond strengths, as observed by other authors that tested bars with the same rib geometry and different spacings.[16,50] As indicated in Table 3, QST bars have the largest clear spacing amongst the considered bars, followed by CW and TB bars (8.17, 6.83, and 6.38 mm, respectively). This explains the highest results for QST bars. The width of the rib can influence the results as the ratio of c_{clear}/s_R determines the proportion of the perimeter per unit of length occupied by concrete keys: 0.65 for QST bars, 0.57 for CW bars, and 0.64 for TB. Another factor

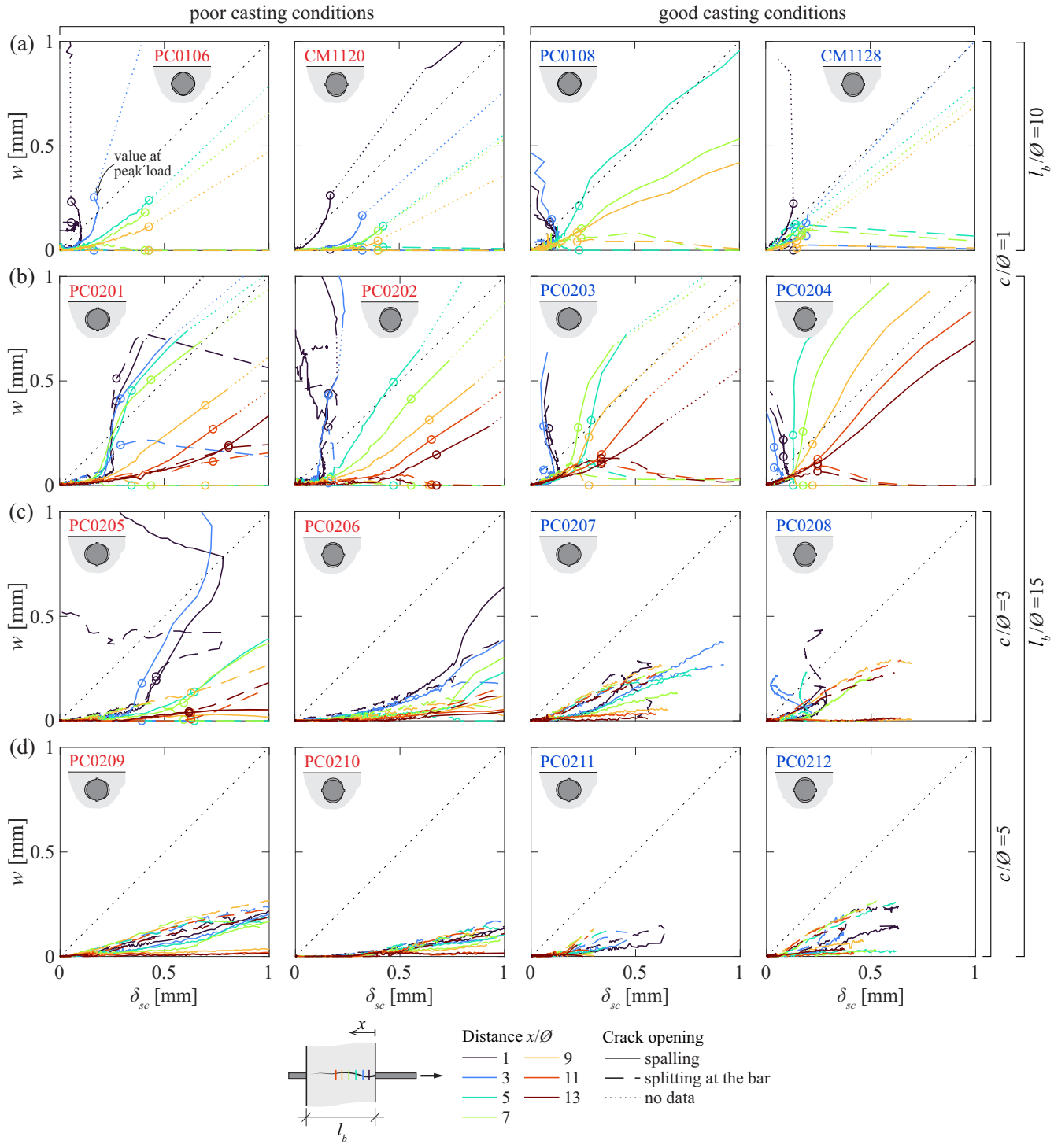

FIGURE 13 Spalling crack opening and splitting crack opening at the bar surface as a function of the local slip for specimens with covers of (a) 1Ø and $l_b/Ø = 10$ (CM1120, 28, PC0106 and 08), (b) 1Ø and $l_b/Ø = 15$ (PC0201 to 04), 3Ø and $l_b/Ø = 15$ (PC0205 to 08) and 5Ø and $l_b/Ø = 15$ (PC0209 to 12).

influencing the bond behavior is the transverse rib angle (β), as previously observed by Soretz et al.,[51] who reported a small increase in the bond performance with increasing inclination of the lugs using pull-out tests on cubes. The higher transverse rib angle for TB bars can increase the bond strength. Consequently, the differences in the measured responses are likely the result of the combination of the aforementioned effects.

4 | RESULT DISCUSSION

4.1 | Splitting and spalling crack evolution

Figure 13 shows the evolution of the spalling crack opening (solid curves) and of the splitting crack opening at the bar surface (dashed curves) as a function of the local slip at different locations along the bar for different specimens. As shown in Figure 13a,b, specimens with low confinement display similar trends regardless of the type of bar, anchorage length, and casting conditions. For small slip values (around 0–0.1 mm), both crack openings remain small and comparable. For larger slip values, the spalling crack becomes significantly larger in most specimens, particularly after the peak load is reached (circles). The crack widths are comparable to the local slip values within a distance of around 7Ø from the loaded end and gradually decrease for locations closer to the unloaded end. However, the values at the peak load are considerably larger for the specimens in poor casting conditions. This indicates a lower stiffness in the spalling mechanism, which can be explained by the presence of plastic settlement cracks.[38] In good casting conditions, the cracks develop and propagate suddenly close to the peak load, which explains the more brittle behavior. Only small differences can be observed due to the rib orientation. Specimens with $QST_{//}$ bars (PC0201 and 03) display slightly larger splitting crack widths than $QST_{\perp}$ specimens (PC0202 and 04).

Figure 13c presents the results for specimens with a cover of 3Ø and shows a clear effect of the conical cracks noticeable in the sudden change of tendency of the spalling crack propagation. For example, in specimen PC0205, the concrete cone breakout causes large spalling cracks at 1 and 3Ø from the loaded end, and a second conical crack causes an increase in the spalling crack width after the peak load for locations at 5 and 7Ø (see Figure 8c,d). For the rest of the locations, the splitting crack increases almost linearly with the slip, and very small spalling openings are measured. The fiber signal is lost before the maximum force for specimens PC0207 to 12. Figure 13d shows the results for specimens with a cover of 5Ø. For most locations, both splitting and spalling cracks follow a fairly uniform tendency and with smaller crack widths than specimens with a cover of 3Ø. It must be noted that for similar slip values, specimens with larger covers reach higher bond stresses, as shown in Figure 7a. No clear trend can be observed due to the rib orientation.

4.2 | Local bond–slip relationship

4.2.1 | Well-confined conditions

The findings presented in the previous sections indicate that the local bond–slip relationship from MC2010 underestimates the stiffness of the local bond response. The pre-peak response is controlled by the maximum bond stress ($\tau_{b,max}$) and the corresponding slip ($\delta_{sc}(\tau_{b,max})$). A database of experimental results from the literature with short bonded lengths, well-confined conditions (MC2010 considers well-confined conditions without transverse reinforcement for $c \geq 5Ø$), and pull-out failure has been collected. All details are provided in Table B1 of Appendix B. The experimental slip at the maximum bond stress is considered equal to the slip at the end of the ascending branch of the local bond–slip relationship (δ_{sc1}, see definitions in Figure 15a).

Concerning the bond strength for good casting conditions, Huang et al.[52] proposed a linear relationship between the compressive strength of concrete and the bond strength based on experimental results with normal and high-strength concrete. This relationship was then adjusted to include the size effect of the bar diameter by Bamonte et al.[53] Nevertheless, based on the existing tests, it seems that a linear relationship tends to overestimate the bond strength for higher concrete compressive strengths. For this reason, accounting also for other considerations,[54] an empirical relationship with a lower exponent is prosed on the basis of the existing experimental results:

$$\tau_{b,max} = 0.93 f_{cm}^{5/6} \left(\frac{20}{Ø}\right)^{1/6}. \quad (2)$$

With respect to the slip at maximum bond stress, Eligehausen et al.[3] observed that it is influenced by the concrete compressive strength and by the clear spacing between ribs. Tepfers et al.[50] proposed an inversely proportional relationship between the peak slip and the bond index. Various linear relationships based on the clear rib spacing have been proposed by other authors.[55–57] On the basis of the existing tests, the ratio between clear rib spacing and bar diameter seems to have a nonnegligible influence. Based on these considerations, the following expression is proposed:

$$\delta_{sc1} = 0.09 (c_{clear} Ø)^{1/2} \left(\frac{30}{f_{cm}}\right)^{1/3} \left(\frac{0.07}{f_R}\right)^{1/3}. \quad (3)$$

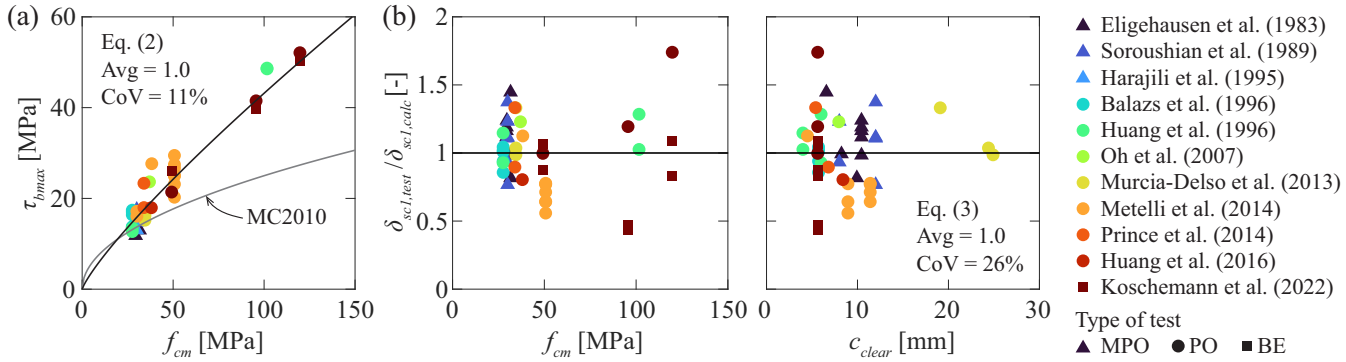

FIGURE 14 Database analysis: (a) maximum local bond stress as a function of the concrete compressive strength; and (b) comparison of measured-to-predicted slip values at the peak bond stress ($\delta_{sc1,test}/\delta_{sc1,calc}$) as a function of the concrete compressive strength and the clear rib spacing (MPO = modified pull-out test, PO = standard pull-out test and BE = beam-end test).

As shown in Figure 14a, Equation (2) describes better the influence of the compressive concrete strength on the bond strength than the MC2010 provision. Figure 14b compares the results of the proposed expression for the slip corresponding to the maximum bond stress with the experimental values. Equation (3) shows good agreement with the database results with a reasonable scatter considering the variability in bond results (Table 1).

Concerning bars in poor casting conditions, Moccia et al.[38,58] measured the size of the voids under reinforcement bars cast in the horizontal position using tomography. They observed larger voids with the increase of the height above the formwork and proposed a method for the quantification of the bond strength of horizontal bars in poor casting conditions, estimating the size of the voids under the bar using the model by Brantschen et al.[32] that proposes a reduction of the bond strength due to the effect of a longitudinal crack parallel to the bar. The reduction factor is assumed to be proportional to the reduction of the area of contact between the ribs and the surrounding concrete (Figure 15a). The reduction factor is calculated using Equation (4) on the basis of the crack width (w), the nominal bar diameter ($\emptyset$), the bond index (f_R), and a proportionality factor ($\kappa_f = 0.75 \times n_l$) that accounts for the number of lugs that compose the rib (n_l). According to Brantschen et al.,[32] the crack opening leads to an additional slip related to the transverse rib flank inclination (α_R) that can be estimated using Equation (5) (Figure 15b). The void size (in this case, equivalent to the crack width) can be estimated using Equation (6) on the basis of the plastic settlement strain (s_{ps}) and the height above the formwork (h).

$$\eta_2 = \frac{\tau_b}{\tau_{b0}} = \frac{1}{1 + \frac{\kappa_f}{f_R}\frac{w}{\emptyset}}, \tag{4}$$

$$\Delta\delta_{sc} = \frac{w}{2}\cot\alpha_R \le h_R \cot\alpha_R, \tag{5}$$

$$w = h \times s_{ps}. \tag{6}$$

The direct application of these expressions would lead to an initial slip with no activation of bond stresses. In fact, a part of the lugs is likely to remain in contact with the concrete closer to the equator of the bar. Furthermore, chemical adhesion and friction will act in most of the perimeter of the bar.[1] Consequently, the initial slip for poor casting conditions is kept as zero, whereas the other points of the bond–slip relationship are adjusted using Equations (4) and (5). The parameters defining the proposed local bond–slip relationship are summarized in Table 5. The proposal is compared with the original expressions of MC2010 in Figure 15c.

4.2.2 | Low and moderate confinements

The experimental measurements presented in this article show that significant cracking in the bonded region occurs due to bond for covers between 1 and 3Ø. Consequently, for such conditions, the assumption of a reduction of the bond strength caused solely by the existence of plastic settlement cracks can be unrealistic. Equation (4) is a simplification for practical purposes of the actual variation of the contact surface with one crack. The proportionality factor has been calibrated based on numerical analysis for bars with different numbers and types of lugs to provide a satisfactory estimation for the possible different orientations.[59] The experimental results have shown the presence of two sets of cracks approximately parallel to the bar (splitting and spalling cracks). In the following, the ratio between a horizontal splitting

TABLE 5 Parameters defining the proposed and the MC2010 local bond–slip relationships for pull-out failure (for definition of parameters, refer to section Nomenclature and Figure 15c).

	Proposed expressions		MC 2010	
Parameter	**Good casting conditions**	**Poor casting conditions**	**Good casting conditions**	**Poor casting conditions**
$\tau_{b,max}$	Equation (2)	$\eta_2 \times$ (Equation 2)	$2.5 \times f_c^{1/2}$	$2.5 \times \eta_2 \times f_c^{1/2}$
τ_{bf}	$0.40 \times \tau_{b,max}$	$0.40 \times \tau_{b,max}$	$0.40 \times \tau_{b,max}$	$0.40 \times \tau_{b,max}$
δ_{sc1}	Equation (3)	Equation (3) $+ \Delta\delta_{sc}$	1.0 mm	1.8 mm
δ_{sc2}	$2 \times$ (Equation 3)	$2 \times$ (Equation 3) $+ \Delta\delta_{sc}$	2.0 mm	3.6 mm
δ_{sc3}	c_{clear}	$c_{clear} + \Delta\delta_{sc}$	c_{clear}	c_{clear}
α[a]	0.4	0.4	0.4	0.4
η_2	–	Equation (4)	–	0.5
$\Delta\delta_{sc}$	–	Equation (5)	–	–

[a]Parameter α is the exponent for the first branch of the relationship.

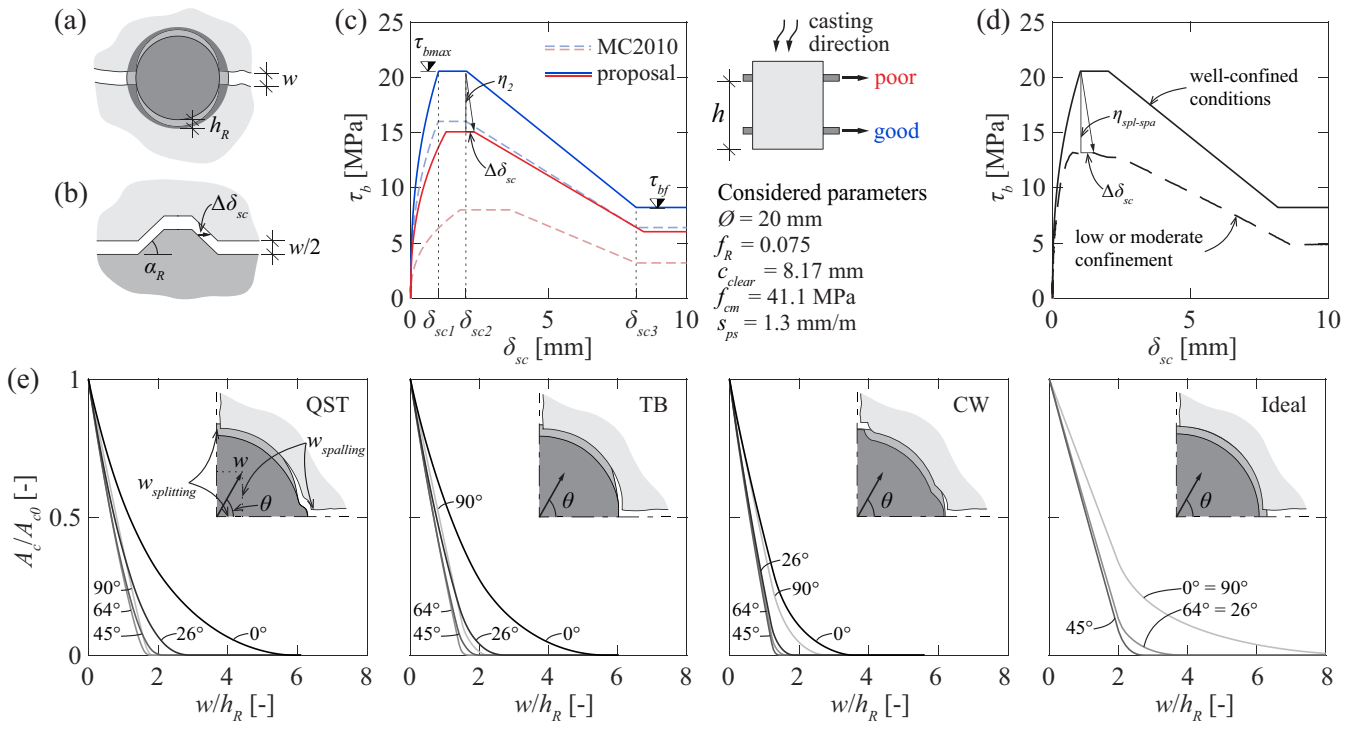

FIGURE 15 Local bond–slip relationship: schematic representation of the effect of a longitudinal crack along the bar: (a) reduction of the lug contact area and (b) slip increment due to the generated gap for an idealized rib geometry; (c) proposed expressions for well-confined conditions compared to MC2010; (d) proposed reduction factor for low or moderate confinement; and (e) rib contact surface reduction for different crack kinematics for QST, TB, CW bars and an idealized rib geometry.

component and a vertical spalling component will be defined by the angle θ (Figure 15e). The two extreme cases considered by Brantschen et al.[32] correspond to the effect of a splitting crack ($\theta = 0°$) or a spalling crack ($\theta = 90°$).

The influence of this parameter in the evolution of the rib contact area (A_c/A_{c0}) for the tested bars and for an idealized geometry is shown in Figure 15e. For all considered rib geometries, the largest reductions correspond to angles of 45° or 64°. For the bars with two lugs (QST and TB), the largest reductions are similar to the case of 90°. However, for the CW bar with four lugs and the idealized rib geometry, the reduction is significantly larger for $\theta = 45°$ (splitting and spalling cracks with the identical opening). Consequently, a coefficient κ_m is introduced in Equation (4) with a value of 1.3 to account

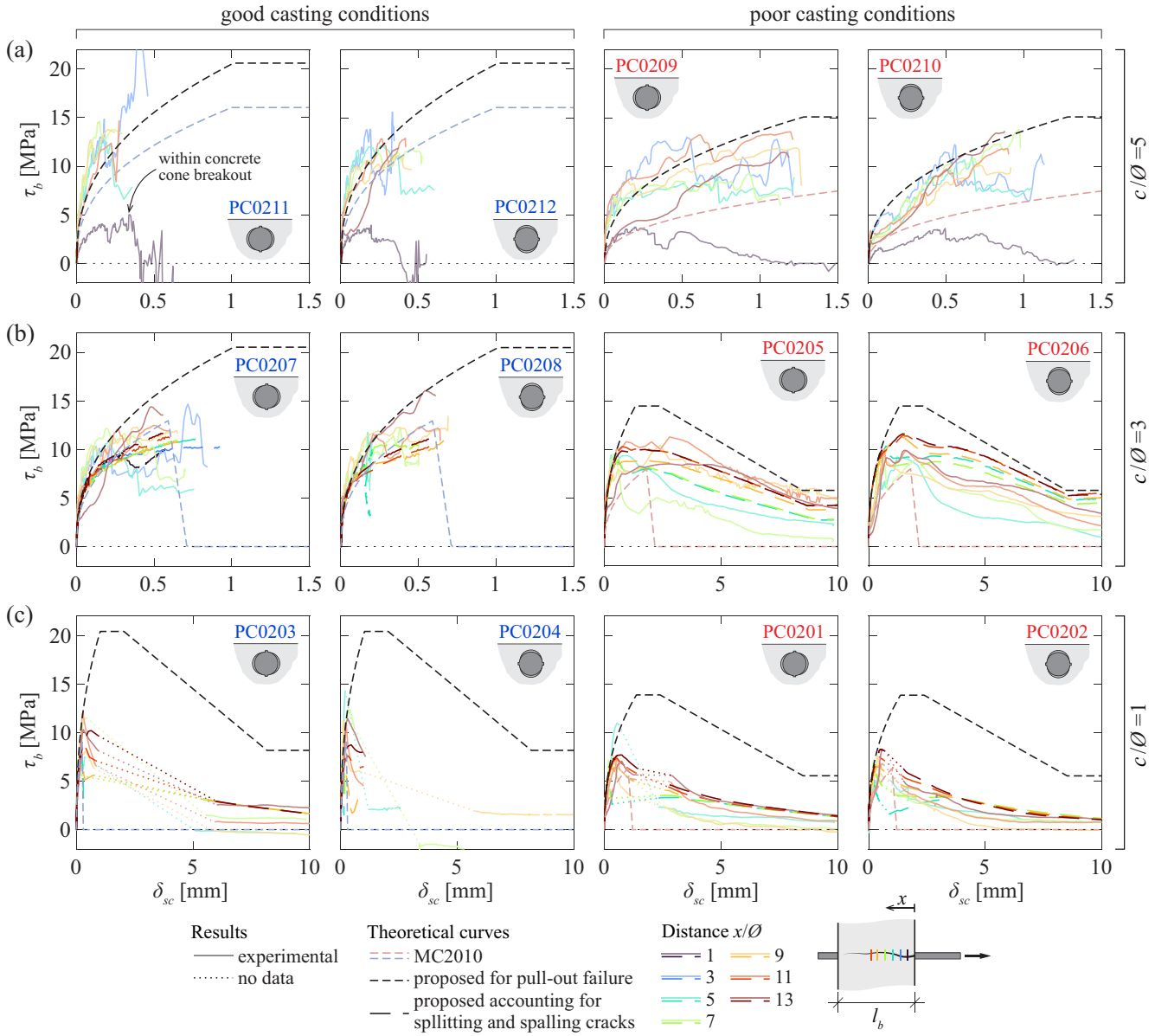

FIGURE 16 Comparison of the analytical model predictions for specimens with covers of (a) 5Ø (PC0209–12); (b) 3Ø (PC0205–08); and (c) 1Ø (PC0201–04).

for cases with multiple cracks. The resulting bond strength reduction factor (Figure 15d) is:

$$\eta_{\text{spl-spa}} = \frac{\tau_b}{\tau_{b0}} = \frac{1}{1+\frac{\kappa_f \kappa_m}{f_R}\frac{w}{Ø}}. \quad (7)$$

4.3 | Comparison to test results

Figure 16a compares the model for well-confined conditions with the local measurements from specimens PC0209 to 12 with a cover of 5Ø. For good casting conditions, the proposal follows better the measured response within the region not affected by the cone breakout. In this case, the stiffness of the response remains slightly underestimated. The smaller bond stresses measured for specimen PC0212 can be explained by the larger crack widths measured (Figure 13d). The theoretical bond–slip relationship for poor casting conditions plotted in Figure 16a has been calculated assuming a plastic settlement of 1.3 mm/m (estimated void size ≈ 0.36 mm).[38] They show a relatively fine agreement with the test results (average response between the results of the two bar orientations). The local bond–slip measurements from specimens PC0209 and 10 justify the absence of an initial slip in poor casting conditions.

Specimen PC0209 ($QST_{//}$) displays a uniform trend with a shape similar to the curves of MC2010. Specimen PC0210 ($QST_{\perp}$) follows a similar trend for bond stresses below 3–4 MPa, after which the trend changes, leading to larger slips for comparable bond stresses. The difference is probably caused by plastic settlement voids that affect more the $QST_{\perp}$ bars.

For low and moderate confinements, the crack evolution presented in Figure 13b,c shows comparable splitting and spalling cracks for most of the bonded length, particularly before the peak force. On this basis, Equation (7) has been applied for specimens PC0201 to 08 with QST bars using as reference the proposed bond–slip relationship for well-confined conditions (dashed black line) and the local crack opening measurements. The crack width considered in the reduction factor corresponds to the magnitude of the vector addition of the splitting and spalling crack components. The resulting estimated local bond–slip relationships (dashed lines) are displayed in Figure 16b,c, and compared with the experimental measurements (solid lines). The results within the concrete cone breakout (typically from the loaded end up to a distance of around 3Ø and shown in the dark gray hatch in Figure 8) are not considered, as the assumption of the reference curve is not realistic. In general, the analytical results capture well the tendencies of the experimental measurements, whereas the corresponding local bond–slip relationships provided in MC2010 (light red and blue dashed lines) differ significantly from the experimental results, particularly in the post-peak range.

Describing the bond–slip relationship for unconfined conditions as a function of the measured splitting and spalling cracks can be useful to estimate the steel stress as a function of the measured cracks in case of assessment of existing structures (to estimate the risk of fatigue or the residual resistance of anchorages affected by longitudinal cracks due to corrosion for instance). In addition, this can be seen as a step forward in the development of a fully mechanical model to calculate the bond stress at SLS and the anchorage resistance at ULS in a more rational manner.

5 | CONCLUSIONS

This paper presents the results of an experimental program and an analytical investigation to characterize the local bond–slip relationship along anchored bars of medium length and to establish a mechanical model to describe the effect of plastic settlement voids and cracking visible on the concrete surface on the local bond–slip relationship. The main findings of this research are summarized below:

1. The bond behavior in structural elements is complex, and the study of elements with medium and long anchorages is necessary to complement the experiments with short bonded lengths.
2. Fiber optical sensors in combination with DIC have proven to be useful to study the distribution of steel stresses and bond stresses along the anchorage length, the local bond–slip response and the influence of cracks visble in the concrete surface. The experimental results show that cracking has an unfavourable effect on the bond performance of anchored bars.
3. The effect of concrete cover and casting direction on the bond strength agrees with previous research. The anchorage resistance increases for larger covers. The largest anchorage resistance is obtained for bars in good casting conditions, followed by bars loaded in the opposite direction of casting, and then by bars loaded in the casting direction. The lowest resistance is obtained for bars in poor casting conditions.
4. The effect of the rib orientation with respect to the concrete surface is more relevant for anchorages with low covers governed by the spalling of the concrete cover. In well-confined conditions, the anchorage resistance of bars with similar bond indexes but different rib geometries can differ by more than 15%. In such conditions, the anchorage response is not sufficiently well characterized, accounting only for the bond index.
5. In specimens with medium anchorage lengths and moderate or well-confined conditions, the behavior is less brittle, and the effect of the redistribution of bond forces due to a lower stiffness of the local bond response can lead to a higher anchorage resistance, even if lower local bond stresses are activated.
6. The measured local bond–slip relationships show higher stiffness than the MC2010 expressions for all the tested conditions and parameters. Specimens with a cover of 3Ø do not display such a brittle post-peak response as the corresponding unconfined splitting failure proposed in MC2010. They failed by splitting induced pull-out developing bond stresses even for slip values similar to the rib spacing.
7. A local bond–slip model for deformed bars with pull-out failure (well-confined conditions) is proposed based on the analysis of a database of tests collected from the literature. The model for poor casting conditions is derived based on mechanical considerations due to the voids under the bar caused by plastic settlement.

8. The differences in the local bond–slip response for low and moderate confinements, with respect to the pull-out failure, can be explained by the development of spalling cracks (parallel to the bar and approximately parallel to the concrete surface), splitting cracks (parallel to the bar and approximately perpendicular to the concrete surface), and conical cracks leading to concrete cone breakouts near the loaded end of the bar.
9. For these phenomena, a simple model is proposed to quantify the bond strength reduction as a function of the measured opening of longitudinal cracks in the bonded region.

NOMENCLATURE

b	rib width
c	clear concrete cover
c_{clear}	clear rib spacing
f_c	cylinder compressive strength of concrete
f_R	bond index
f_t	tensile strength of reinforcement
f_y	yield strength of reinforcement
h	distance from the bar surface to the bottom of the formwork
$h_{R,avg}$	average rib height
$h_{R,max}$	maximum rib height
l_b	bonded length
n_l	number of lugs that compose the rib
n_s	number of transverse reinforcement stirrups
n_t	number tests
s_{ps}	plastic settlement strain
s_R	transverse rib spacing
w	crack width
x	coordinate
A_c	rib contact area
F_{max}	maximum pull-out force
α	exponent for the ascending branch of the bond–slip relationship of MC2010
α_R	transverse rib flank inclination
β	transverse rib angle
δ_s	bar displacement
δ_c	concrete displacement
δ_{sc}	relative slip
$\delta_{sc}(\tau_{b,max})$	slip corresponding to the maximum bond stress
$\delta_{sc,end}$	relative slip at the unloaded end of the bar
δ_{sc1}	slip at the end of the ascending branch of the local bond–slip relationship
δ_{sc2}	slip at the end of the plateau of the local bond–slip relationship
δ_{sc3}	slip at the beginning of the residual frictional branch
ε_s	bar axial strain
η_2	bond stress reduction factor for poor casting conditions
$\eta_{spl\text{-}spa}$	bond stress reduction factor due to splitting and spalling cracks
θ	ratio between splitting and spalling components of the crack width
κ_f	proportionality factor
κ_m	factor to account for the presence of multiple cracks
σ_s	bar axial stress
σ_{sR}	maximum stress at the loaded end of the bar
τ_b	bond stress
τ_{b0}	reference bond stress
$\tau_{b0.1}$	bond stress corresponding to a slip at the unloaded end of 0.1 mm
τ_{bf}	residual frictional bond strength
$\tau_{b,avg}$	average bond stress over the bonded length
$\tau_{b,max}$	maximum bond stress
$Ø$	bar diameter
$Ø_s$	transverse stirrup bar diameter

ACKNOWLEDGMENTS

This work was performed within the frame of the research project AGB/2019/017 of the Swiss Federal Roads Authority (FEDRO), whose support is acknowledged. Open access funding provided by Ecole Polytechnique Federale de Lausanne.

DATA AVAILABILITY STATEMENT

The data that support the findings of this study are available from the corresponding author upon reasonable request.

REFERENCES

1. fib Bulletin. *fib* Bulletin no. 10: Bond of reinforcement in concrete. State-of-art report. Lausanne, Switzerland: Fédération Internationale du Béton. 2000.
2. Lindorf A. Ermüdung des Verbundes von Stahlbeton unter Querzug. Dresden, Germany: Technischen Universität Dresden, Fakultät Bauingenieurwesen. 2011.
3. Eligehausen R, Popov P, Bertero V. Local bond stress-slip relationships of deformed bars under generalized excitations. UCB/EERC 83/23. 1983.
4. Shima H, Chou L-L, Okamura H. Micro and macro models for bond in reinforced concrete. J Fac Eng Univ Tokyo. 1987;39:133–94.
5. Giurani E, Plizzari G. Interrelation of splitting and flexural cracks in RC beams. J Struct Eng. 1998;124(9):1032–40.
6. Idda K. Verbundverhalten von Betonrippenstählen bei Querzug. Karlsruhe, Germany: Institut für Massivbau und Baustofftechnologie, Universität Karlsruhe. 1999.
7. fib. *fib* Model Code for concrete structures 2010. UK: fib; 2013.
8. CEN. Eurocode 2: Design of concrete structures-Part 1-1: general rules and rules for buildings. Brussels, Belgium: European Committee for Standardization (CEN). 2004.
9. SIA. SIA 262:2013—Structures en béton, Société suisse des ingénieurs et des architectes. Zurich, Switzerland: SIA. 2013.

10. Plizzari G, Metelli G, Cairns J. An overview of enhancements to provisions for bond in the draft *fib* Model Code 2020. Bond in Concrete 2022. Stuttgart, Germany. 2022.
11. CEN. Eurocode 2: Design of concrete structures-Part 1-1: general rules and rules for buildings, bridges and civil engineering structures, Final draft FprEN 1992-1-1. Brussels, Belgium: European Committee for Standardization (CEN). 2023.
12. Muttoni A, Cairns J, Goodchild C, Ganz HR. Background document to clauses 11.4 and 11.5—Anchorage and laps of bars in tension and compression. Lausanne, Switzerland. 2023.
13. fib. *fib* Bulletin no. 72: Bond and anchorage of embedded reinforcement: background to the *fib* Model Code for concrete structures 2010. Lausanne, Switzerland: Fédération Internationale du Béton. 2014.
14. RILEM. Essais portant sur l'adhérence des armatures du béton—Essais par traction, Recommandation RILEM/CEB/FIP-RC6. Matériaux et Constructions. 1978;6:32.
15. Goto Y. Cracks formed in concrete around deformed tension bars. ACI J. 1971;68(4):244–51.
16. Metelli G, Plizzari G. Influence of the relative rib area on bond behaviour. Mag Concr Res. 2014;66(6):277–94.
17. Cantone R, Fernández Ruiz M, Muttoni A. A detailed view on the rebar-to-concrete interaction based on refined measurement techniques. Eng Struct. 2021;226:111332.
18. Koschemann M, Curbach M, Marx S. Investigation of local bond behavior using distributed optical fiber sensing, Bond in Concrete 2022. Stuttgart, Germany. 2022.
19. Lemcherreq Y, Galkovski T, Mata Falcón J, Kaufmann W. Application of distributed fibre optical sensing in reinforced concrete elements subjected to monotonic and cyclic loading. Sensors. 2022;22(5):28.
20. Cairns J, Plizzari G. Towards a harmonised European bond test. Mater Struct. 2003;36:498–506.
21. ASTM. ASTM A944-10. Standard test method for comparing bond strength of steel reinforcing bars to concrete using beam-end specimens. USA: ASTM International. 2015.
22. Koschemann M, Curbach M, Marx S. Influence of the test setup on the local bond behaviour of ribbed steel bars. *fib* International Congress 2022. Norway. 2022.
23. Mains RM. Measurement of the distribution of tensile and bond stresses along reinforcing bars. J Am Concr Inst. 1951;23(3):225–52.
24. Djabry W. Contribution à l'étude de l'adhérence des fers d'armature au béton, Rapport EMPA N°184. Zürich: EMPA. 1952.
25. Nilson AH. Internal measurement of bond slip. ACI J. 1972;69(7):439–41.
26. Bado MF, Casas J-R, Kaklauskas G. Distributed sensing (DOFS) in reinforced concrete members for reinforcement strain monitoring, crack detection and bond-slip calculation. Eng Struct. 2021;226:111385.
27. Balázs GL. Cracking analysis based on slip and bond stresses. ACI Mater J. 1993;90:340–8.
28. CEB. *fib* Model Code 1990. London, UK: Comité Euro-International du Béton (CEB). 1993.
29. Fernández RM, Muttoni A, Gambarova P. Analytical modelling of the pre- and post-yield behaviour of bond in reinforced concrete. ASCE J Struct Eng. 2007;133(10):1364–72.
30. Gambarova P, Paolo Rostasi G, Zasso B. Steel-to-concrete bond after concrete splitting: constitutive laws and interface deterioration. Mater Struct. 1989;22(131):347–56.
31. Mahrenholtz C. Seismic bond model for concrete reinforcement and the application to column-to-foundation connections, Stuttgart, Germany: Universität Stuttgart, Institut für Werkstoffe im Bauwesen. 2012.
32. Brantschen F, Faria DMV, Fernández Ruiz M, Muttoni A. Bond behaviour of straight, hooked, U-shaped and headed bars in cracked concrete. Struct Concr. 2016;17(5):799–810.
33. Moccia F, Fernández Ruiz M, Muttoni A. Spalling of concrete cover induced by reinforcement. Eng Struct. 2021;237:112188.
34. ISO. ISO 15630-1:2019: Steel for the reinforcement and prestressing of concrete—test methods—part 1: reinforcing bars, wire rod and wire, International Organization for Standardization. 2019.
35. Correlated Solutions. Vic-3D 8 Software Manual, Version 8.4. 2021.
36. Luna Technologies Inc. ODiSI 6000 Series User Guide. 2020.
37. Galkovski T, Lemcherreq Y, Mata Falcón J, Kaufmann W. Fundamental studies on the use of distributed fibre optical sensing on concrete and reinforcing bars. Sensors. 2021;21(22):24.
38. Moccia F, Fernández Ruiz M, Metelli G, Muttoni A, Plizzari G. Casting position effects on bond performance of reinforcement bars. Struct Concr. 2021;22:1612–32.
39. Bado MF, Casas J-R, Dey A, Berrocal C, Kaklauskas G, Fernandez I, et al. Characterization of concrete shrinkage induced strains in internally-restrained RC structures by distributed optical fiber sensing. Cem Concr Compos. 2021;120:104058.
40. Clark AP. Bond of concrete reinforcing bars. J Res Natl Bureau Standards. 1949;43:565–79.
41. Rehm G. Über die Grundlagen des Verbunds zwischen Stahl und Beton. Berlin: Deutscher Ausschuss für Stahlbeton. 1961.
42. Martin H, Noakowski P. Verbundverhalten von Betonstahlen Untersuchung auf der Grundlage von Ausziehversuchen. Berlin: Deutscher Ausschuss für Stahlbeton. 1981.
43. Pérez Caldentey A, García R, Gribiniak V, Rimkus A. Tension versus flexure: reasons to modify the formulation of MC 2010 for cracking. Struct Concr. 2020;21(5):2101–23.
44. Gehri N, Mata-Falcón J, Kaufmann W. Refined extraction of crack characteristics in large-scale concrete experiments based on digital image correlation. Eng Struct. 2022;251:113486.
45. Kreller H. Zum nichtlinearen Trag-und Verformungsverhalten von Stahlbetonstabtragwerken unter Last-und Zwangeinwirkung. Institut für Werkstoffe im Bauwesen, Mitteilungen, Universität Stuttgart. 1989.
46. Corres E, Muttoni A. Validation of bond models for the crack width estimation based on detailed measurements, 14th *fib* International PhD Symposium in Civil Engineering. 2022.
47. Cairns J, Jones K. Influence of rib geometry on strength of lapped joints: an experimental and analytical study. Mag Concr Res. 1995;47(172):253–62.
48. Cairns J. Top cast effect: influence of bond length on splitting mode failure. Struct Concr. 2022;23(5):2696–709.
49. Corres E, Muttoni A. Long anchorage resistance of reinforcement bars derived from local bond-slip relationships for good and poor bond conditions. Bond in Concrete 2022. Stuttgart, Germany. 2022.
50. Tepfers R, Olsson P-A. Ring test for the evaluation of bond properties of reinforcing bars. Bond in Concrete—from Research to Practice. 1992.

51. Soretz S, Holzenbein H. Influence of rib dimensions of reinforcing bars on bond and bendability. ACI J Proc. 1979;76(1): 111–28.
52. Huang Z, Engström B, Magnusson J. Experimental and anatycal studies of the bond behaviour of deformed bars in high strength concrete. Proceeding ot the 4th Int. Symp. on utilization of high strength/high performance concrete. Paris, France. 1996.
53. Bamonte P, Gambarova P. High-bond bars in NSC and HPC: study on size effect and on the local bond stress-slip law. ASCE J Struct Eng. 2007;133(2):225–34.
54. Moccia F, Yu Q, Fernández Ruiz M, Muttoni A. Concrete compressive strength: from material characterization to a structural value. Struct Concr. 2021;22:E634–54.
55. Harajli MH, Maalouf D, Khatib H. Effect of fibers on the punching shear strength of slab-column connections. Cem Concr Compos. 1995;17:161–70.
56. Zhao W, Zhu B. Theoretical model for the bond–slip relationship between ribbed steel bars and confined concrete. Struct Concr. 2017;19(2):548–58.
57. Lin H, Zhao Y, Ozbolt J, Feng P, Jiang C, Eligehausen R. Analytical model for the bond stress-slip relationship of deformed bars in normal strength concrete. Construct Build Mater. 2019; 198:570–86.
58. Moccia F, Kubski X, Fernández Ruiz M, Muttoni A. The influence of casting position and disturbance induced by reinforcement on the structural concrete strength. Struct Concr. 2021; 22:E655–82.
59. Brantschen F. Influence of bond and anchorage conditions of the shear reinforcement on the punching strength of RC slabs, Thèse n°7315. Lausanne, Suisse: EPFL. 2016.
60. Soroushian P, Choi K-B. Local bond of deformed bars with different diameters in confined concrete. ACI Struct J. 1989;86(2): 217–22.
61. Harajli MH, Hout M, Jalkh W. Local bond stress-slip behaviour of reinforcing bars embedded in plain and fibre concrete. ACI Mater J. 1995;92(4):343–54.
62. Balázs GL, Grosse CU, Koch R, Reinhardt HW. Damage accumulation on deformed steel bar to concrete interaction detected by acoustic emission technique. Mag Concr Res. 1996;48(177): 311–20.
63. Oh BH, Kim SH. Realistic models for local bond stress-slip of reinforced concrete under repeated loading. J Struct Eng. 2007; 133(2):216–24.
64. Murcia-Delso J, Stavridis A, Shing PB. Bond strength and cyclic bond deterioration of large diameter bars. ACI Struct J. 2013; 110(4):659–70.
65. Prince JR, Singh B. Bond behaviour between recycled aggregate concrete and deformed steel bars. Mater Struct. 2013;47: 503–16.
66. Huang L, Chi Y, Xu L, Chen P, Zhang A. Local bond performance of rebar embedded in steel-polypropylene hybrid fiber reinforced concrete under monotonic and cyclic loading. Construct Build Mater. 2016;103:77–92.

AUTHOR BIOGRAPHIES

Enrique Corres, PhD candidate, Ecole Polytechnique Fédérale de Lausanne, School of Architecture Civil and Environmental Engineering Lausanne, Switzerland. Email: enrique.corressojo@epfl.ch.

Aurelio Muttoni, Professor, Ecole Polytechnique Fédérale de Lausanne, School of Architecture Civil and Environmental Engineering Lausanne, Switzerland. Email: aurelio.muttoni@epfl.ch.

How to cite this article: Corres E, Muttoni A. Bond of steel reinforcement based on detailed measurements: Results and interpretations. Structural Concrete. 2023. https://doi.org/10.1002/suco.202300324

APPENDIX A: PULL-OUT TEST RESULTS

Detailed measurements for all tests are shown in Figures A1–A6.

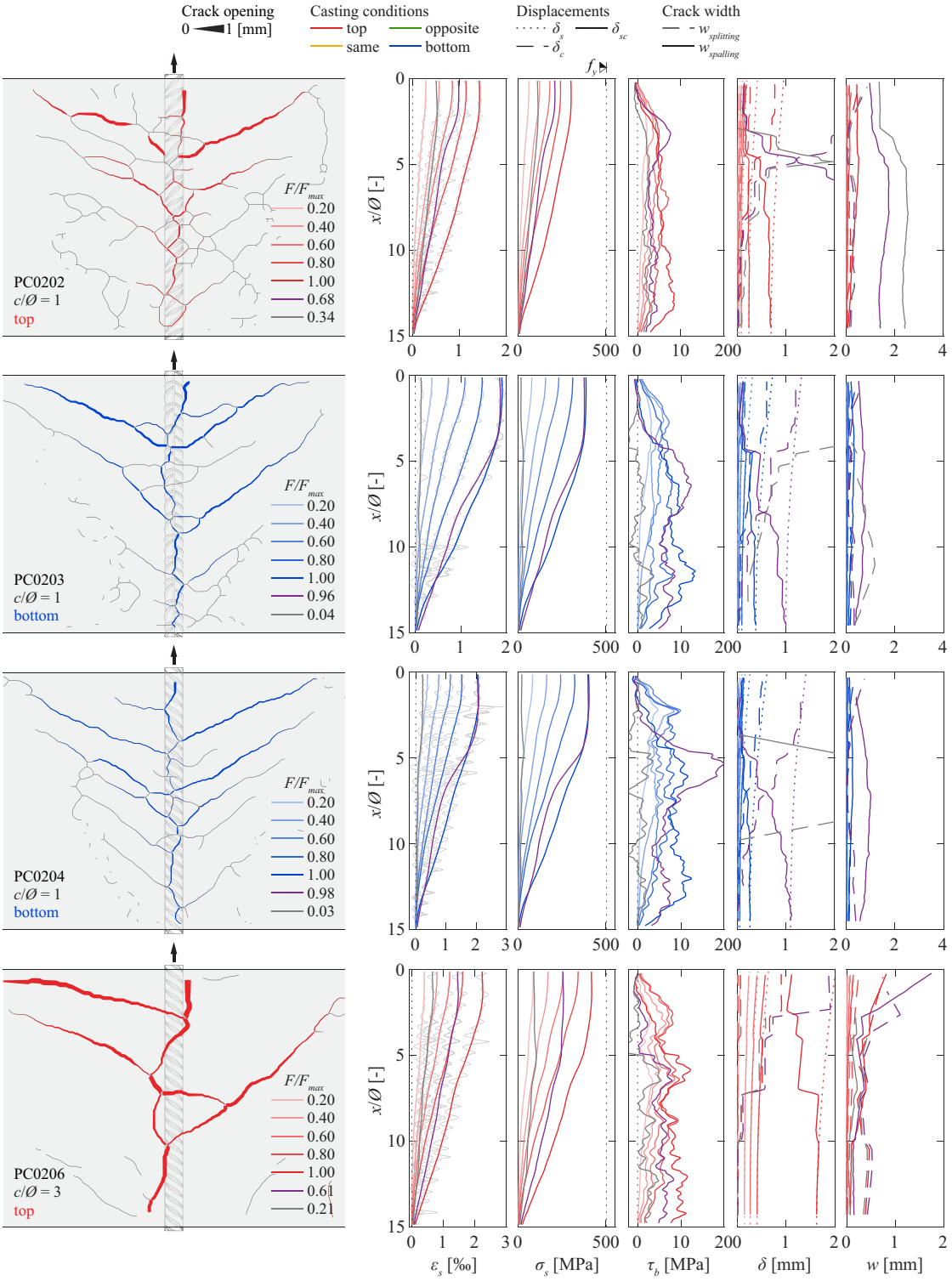

FIGURE A1 Crack pattern and distribution along the anchorage length of axial steel strains, axial steel stresses, bond stresses, slip, and crack widths for specimens: PC0202, PC0203, PC0204, and PC0206.

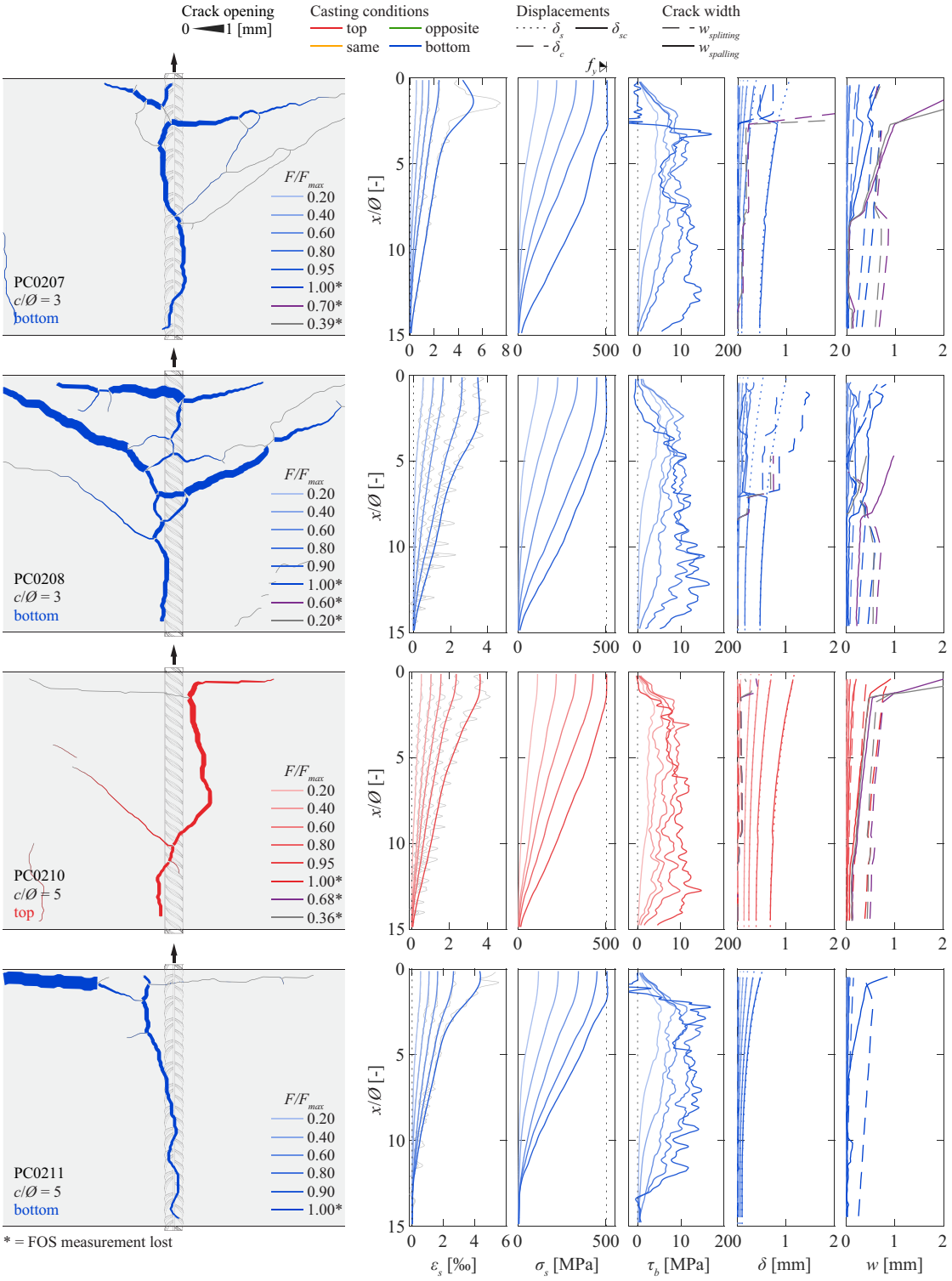

FIGURE A2 Crack pattern and distribution along the anchorage length of axial steel strains, axial steel stresses, bond stresses, slip, and crack widths for specimens: PC0207, PC0208, PC0210, and PC0211.

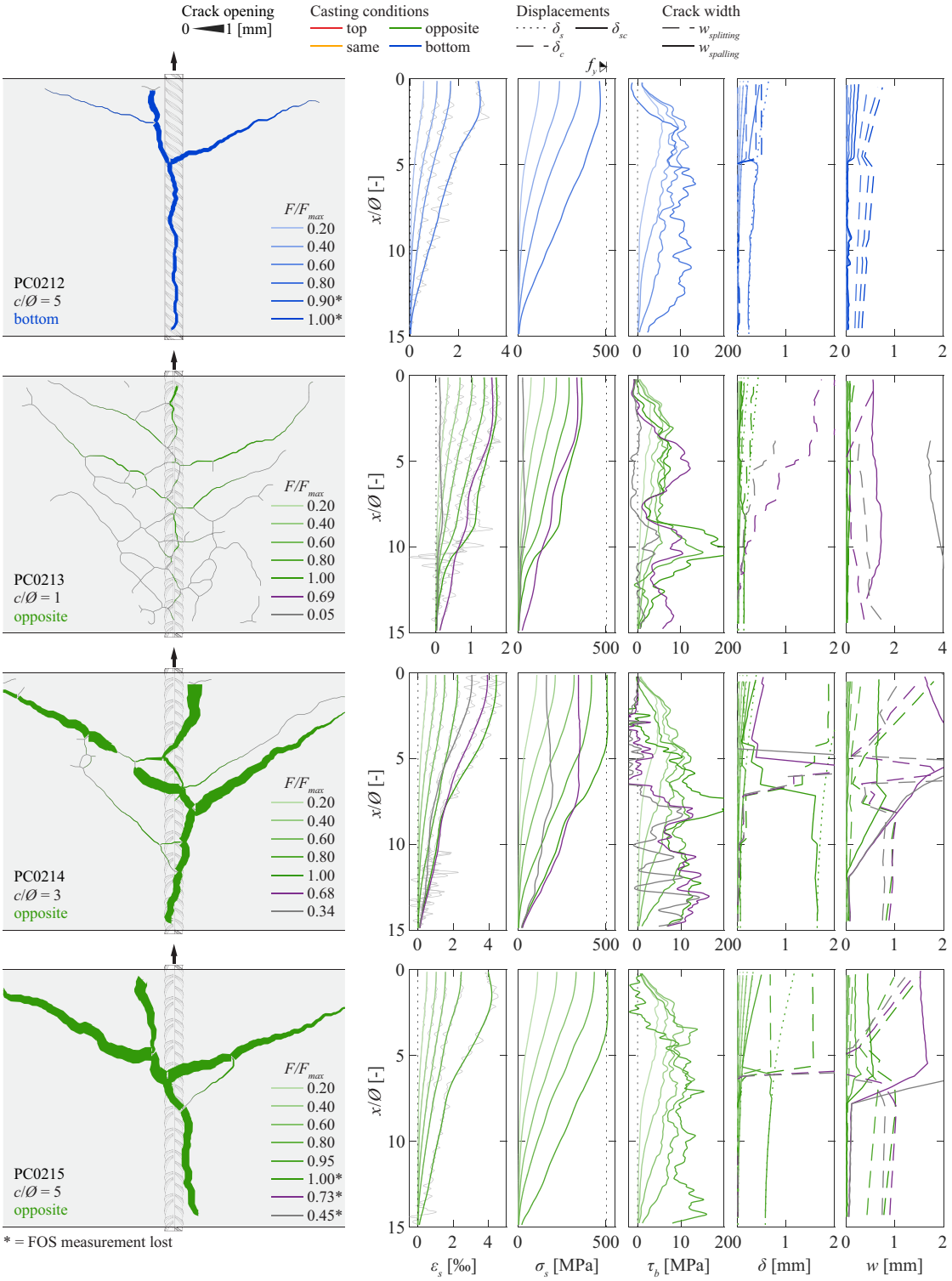

FIGURE A3 Crack pattern and distribution along the anchorage length of axial steel strains, axial steel stresses, bond stresses, slip, and crack widths for specimens: PC0212, PC0213, PC0214, and PC0215.

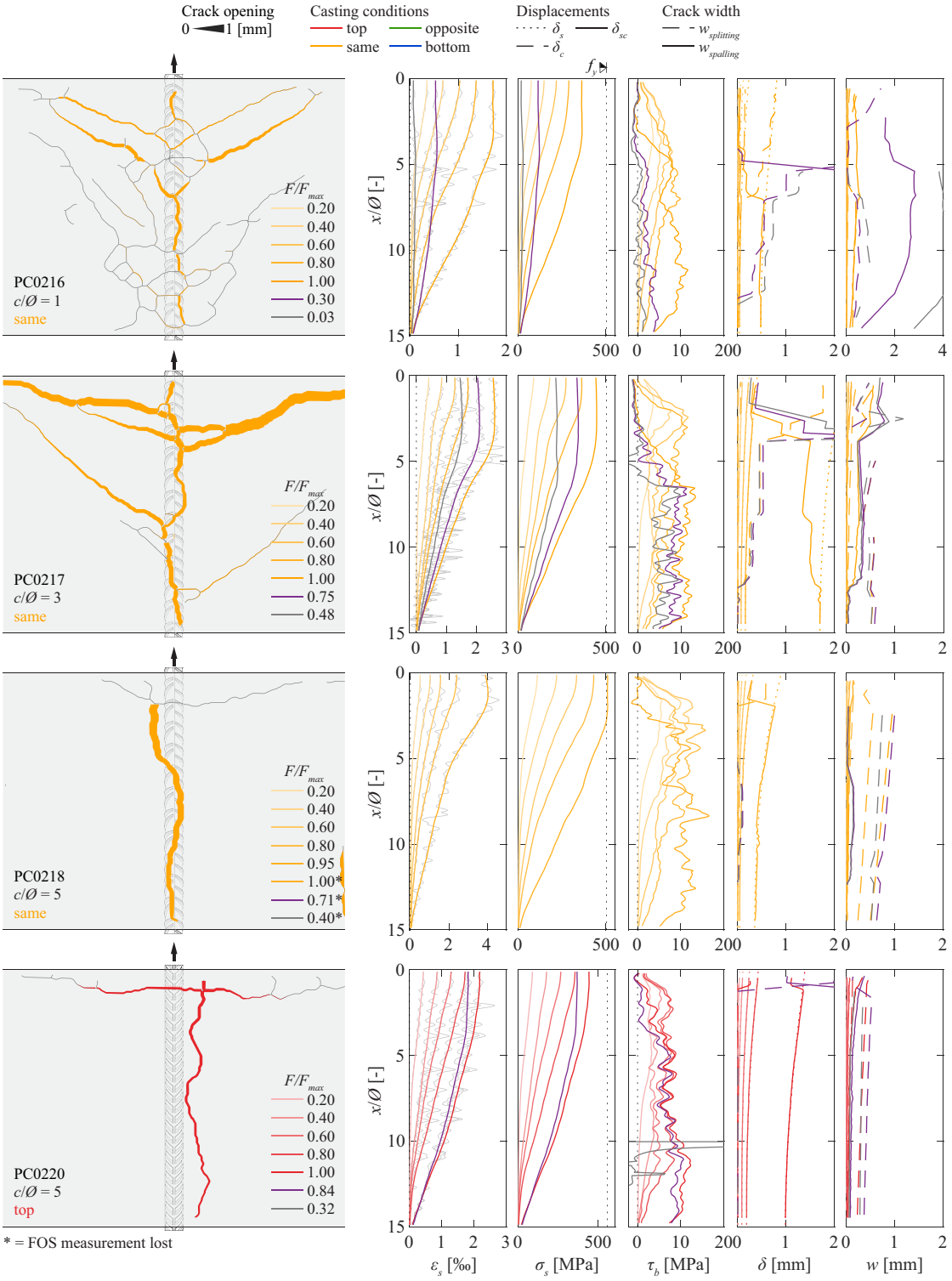

FIGURE A4 Crack pattern and distribution along the anchorage length of axial steel strains, axial steel stresses, bond stresses, slip, and crack widths for specimens: PC0216, PC0217, PC0218, and PC0220.

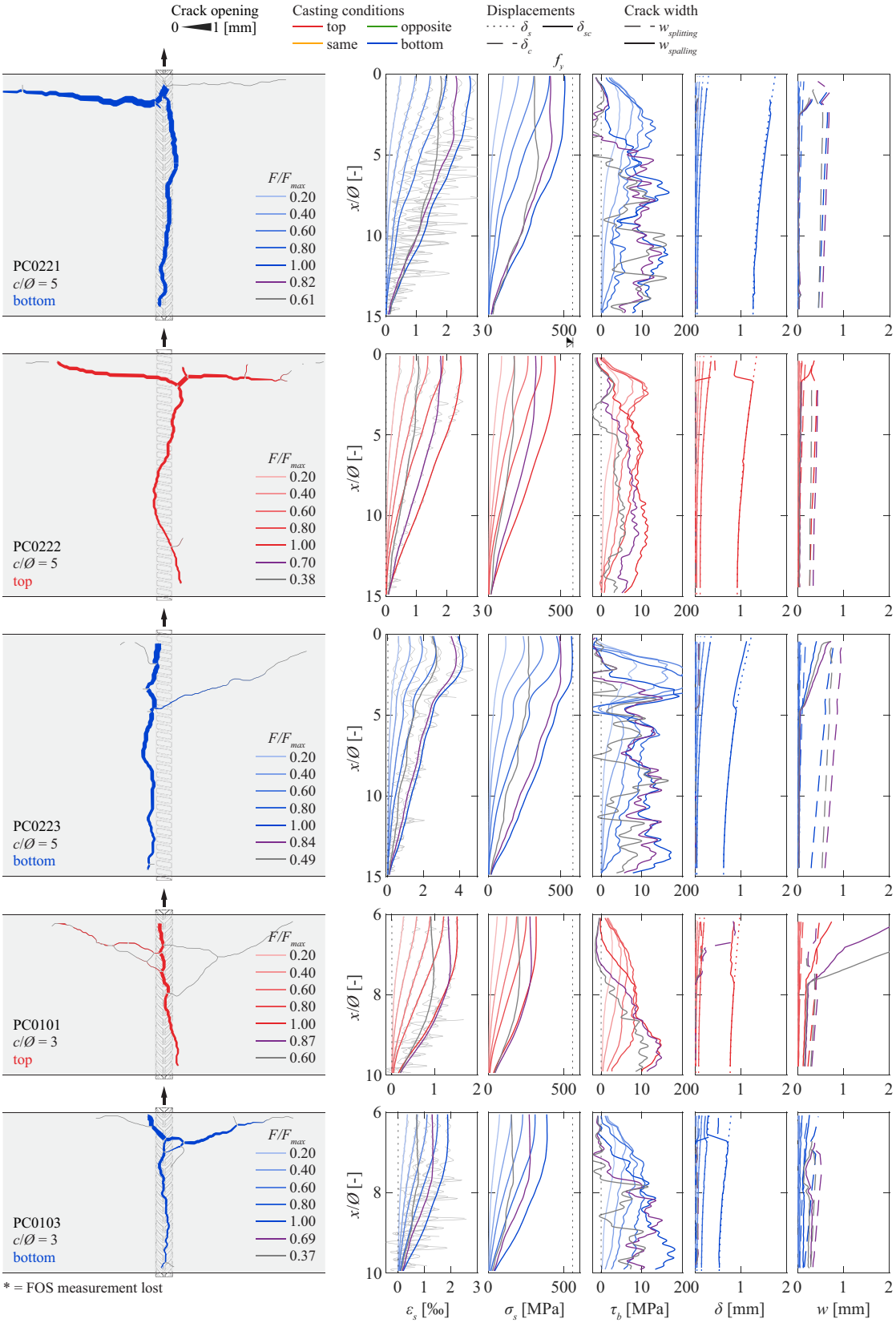

FIGURE A5 Crack pattern and distribution along the anchorage length of axial steel strains, axial steel stresses, bond stresses, slip, and crack widths for specimens: PC0221, PC0222, PC0223, PC0101, and PC0103.

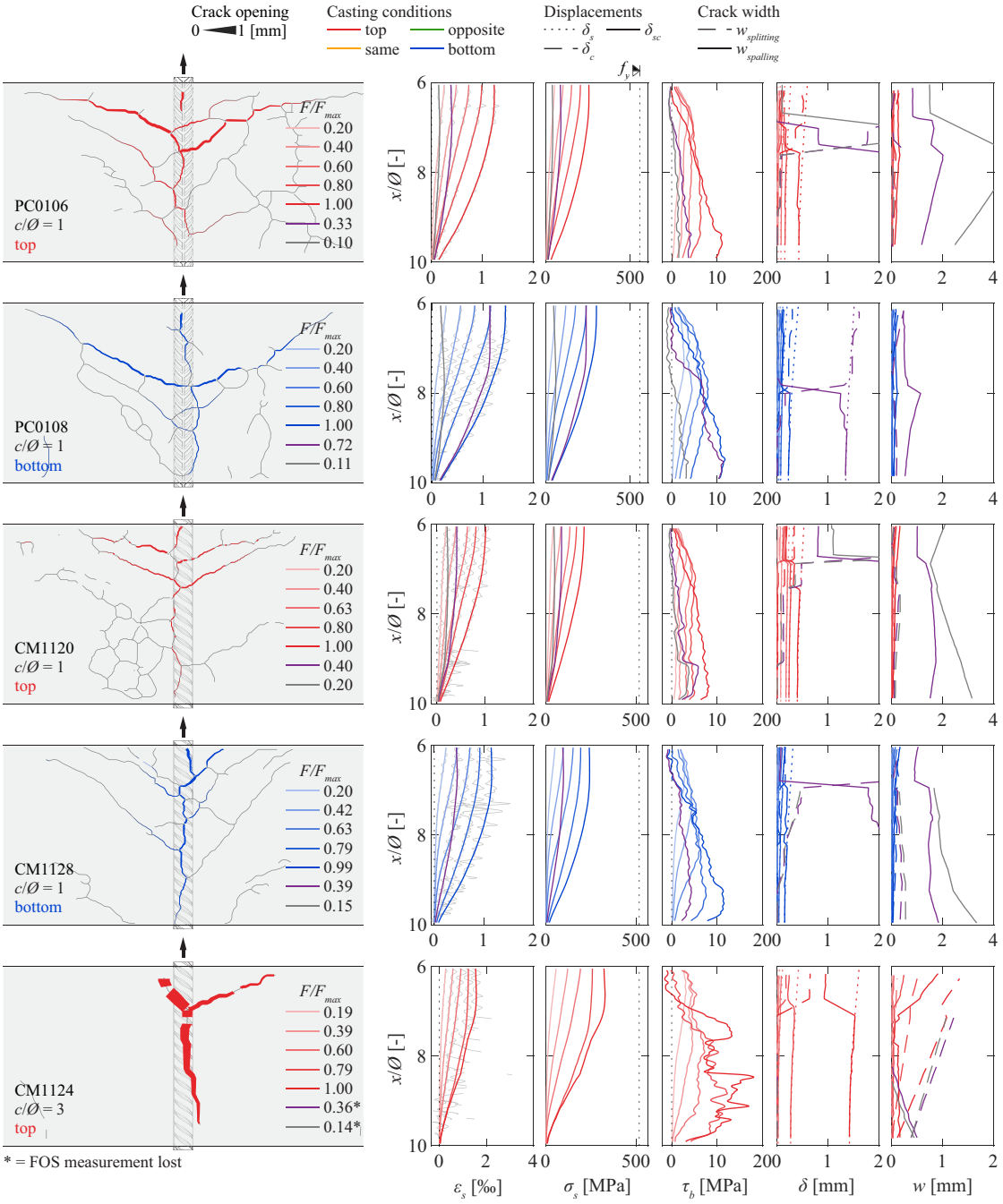

FIGURE A6 Crack pattern and distribution along the anchorage length of axial steel strains, axial steel stresses, bond stresses, slip, and crack widths for specimens: PC0106, PC0108, CM1120, CM1128, and CM1124.

APPENDIX B: EXPERIMENTAL DATABASE

TABLE B1 Main parameters of the experimental database of short pull-out tests in well-confined conditions with pull-out failure (for definition of parameters, refer to section Nomenclature).

Reference	Series	Type of test	Type of bar	n_t	Ø (mm)	$c/Ø$	$l_b/Ø$	f_R (mm)	s_R (mm)	c_{clear} (mm)	b (mm)	h_R (mm)	$Ø_s$ (mm)	n_s	f_c (MPa)	δ_{sc1} (mm)	$\tau_{b,max}$ (MPa)	$\delta_{sc1,test}/\delta_{sc1,calc}$	$\tau_{b,max,test}/\tau_{b,max,MC10}$	$\tau_{b,max,test}/\tau_{b,max,calc}$
Eligehausen et al. (1983)[3]	Series 1.1	MPO	C	3	25.4	2.0	5	0.066	14.0	10.4	3.6		25.4	4	29.4	1.79	13.5	1.19	0.99	0.90
	Series 1.2	MPO	C	3	25.4	2.0	5	0.066	14.0	10.4	3.6		12.7	4	29.4	1.48	13.6	0.98	1.00	0.91
	Series 1.3	MPO	C	3	25.4	2.0	5	0.066	14.0	10.4	3.6		6.35	4	29.4	1.68	11.8	1.12	0.87	0.79
	Series 1.5	MPO	C	3	25.4	2.0	5	0.066	14.0	10.4	3.6		12.7	4	29.4	1.75	14.0	1.16	1.03	0.93
	Series 2.1	MPO	C	2	26.4	2.0	5	0.066	14.0	10.4	3.6		12.7	4	29.6	1.90	13.7	1.24	1.01	0.92
	Series 3.1	MPO	C	2	19.1	2.0	5	0.100	9.7	6.6	3.1		12.7	4	31.6	1.27	15.9	1.45	1.13	0.96
	Series 3.2	MPO	C	2	25.4	2.0	5	0.110	13.4	9.9	3.5		12.7	4	31.6	0.99	15.3	0.82	1.09	0.97
	Series 3.3	MPO	C	2	31.8	2.0	5	0.160	13.5	8.2	5.3		12.7	4	31.6	1.08	13.0	0.99	0.93	0.85
Soroushian et al. (1989)[60]	#5-1	MPO	C	1	16.0	2.0	5	0.060	10.0	8.0	2.0	0.6	12.7	4	30.0	1.32	17.6	1.23	1.28	1.07
	#5-2	MPO	C	1	16.0	2.0	5	0.060	10.0	8.0	2.0	0.6	12.7	4	30.0	1.00	17.2	0.93	1.26	1.05
	#7-1	MPO	C	1	22.0	2.0	5	0.080	13.6	12.0	1.6	1.2	12.7	4	30.0	1.55	15.7	1.11	1.15	1.01
	#7-2	MPO	C	1	22.0	2.0	5	0.080	13.6	12.0	1.6	1.2	12.7	4	30.0	1.56	14.9	1.12	1.09	0.96
	#8-1	MPO	C	1	25.0	2.0	5	0.090	14.4	12.0	2.4	1.3	12.7	4	30.0	1.10	14.8	0.77	1.08	0.97
	#8-2	MPO	C	1	25.0	2.0	5	0.090	14.4	12.0	2.4	1.3	12.7	4	30.0	1.97	15.1	1.37	1.10	0.99
Harajili et al. (1995)[61]	P2 Vf = 0	MPO	C	4	20.0	1.4	3.5		8.0	5.9	2.1		10	4	30.0	1.46	13.0	0.00	0.95	0.82
	P1 Vf = 0	MPO	C	4	25.0	1.5	3.5		15.4	12.2	3.2		10	4	30.0	2.96	15.1	0.00	1.10	0.99
Balázs et al. (1996)[62]	Monotonic	PO	C	1	16.0	2.6	1.25	0.065	8.8	5.7	3.0		–	–	27.6	0.78	13.7	0.86	1.05	0.90
	Monotonic	PO	C	1	16.0	2.6	1.25	0.065	8.8	5.7	3.0		–	–	27.6	0.85	13.7	0.94	1.04	0.89
	Monotonic	PO	C	1	16.0	2.6	1.25	0.065	8.8	5.7	3.0		–	–	27.6	0.95	16.4	1.04	1.25	1.07
	Monotonic	PO	C	1	16.0	2.6	1.25	0.065	8.8	5.7	3.0		–	–	27.6	0.93	17.4	1.02	1.33	1.14
	Monotonic	PO	C	1	16.0	2.6	1.25	0.065	8.8	5.7	3.0		–	–	27.6	0.92	17.0	1.01	1.29	1.11
Huang et al. (1996)[52]	N40-K500	PO	C	4	16.0	8.9	2.5	0.056	8.9	6.0			–	–	27.5	0.91	13.4	0.93	1.02	0.88
	N40-Ks60S	PO	C	3	16.0	8.9	2.5	0.127	7.0	4.0			–	–	27.5	0.70	12.7	1.15	0.97	0.83
	H40-K500	PO	C	4	16.0	8.9	2.5	0.056	8.9	6.0			–	–	101.6	0.81	48.5	1.28	1.93	1.07
	H40-Ks60S	PO	C	3	16.0	8.9	2.5	0.127	7.0	4.0			–	–	101.6	0.40	48.7	1.03	1.93	1.07
Oh et al. (2007)[63]	Monotonic	PO	C	1	16.0	4.2	2	0.098	11.6	8.0	3.6	1.1	–	–	37.0	1.04	23.7	1.23	1.56	1.21
Murcia-Delso et al. (2013)[64]	Series1	PO	C	1	36.0	12.2	5	0.070		19.1			13	6	34.5	3.00	15.2	1.33	1.04	0.94
	Series2	PO	C	1	43.0	10.1	5	0.068		24.9			13	7	34.5	2.80	16.2	0.99	1.10	1.03
	Series3	PO	C	2	57.0	7.5	5	0.095		24.4			13	9	34.5	3.00	17.6	1.04	1.20	1.18

(Continues)

TABLE B1 (Continued)

Reference	Series	Type of test	Type of bar	n_t	Ø (mm)	$c/Ø$	$l_b/Ø$	f_R (mm)	s_R (mm)	c_{clear} (mm)	b (mm)	h_R (mm)	$Ø_s$ (mm)	n_s	f_c (MPa)	δ_{sc1} (mm)	$\tau_{b,max}$ (MPa)	$\delta_{sc1,test}/\delta_{sc1,calc}$	$\tau_{b,max,test}/\tau_{b,max,MC10}$	$\tau_{b,max,test}/\tau_{b,max,calc}$
Metelli et al. (2014)[16]	Series 4-30	PO	M	1	12.0	4.5	5	0.075	6.0	4.5	1.5	0.5	–	–	38.3	0.67	27.6	1.13	1.79	1.31
	Series 8-62	PO	M	1	16.0	4.5	5	0.063	11.0	9.0	2.0	0.5	–	–	50.7	0.72	25.0	0.77	1.40	0.98
	Series 8-63	PO	M	1	16.0	4.5	5	0.058	11.0	9.0	2.0	0.5	–	–	50.7	0.62	26.6	0.64	1.50	1.05
	Series 8-64	PO	M	1	16.0	4.5	5	0.066	11.0	9.0	2.0	0.5	–	–	50.7	0.52	27.5	0.56	1.54	1.08
	Series 9-69	PO	M	1	20.0	4.5	5	0.066	13.9	11.4	2.5	0.5	–	–	50.7	0.83	29.5	0.71	1.66	1.20
	Series 9-70	PO	M	1	20.0	4.5	5	0.069	13.9	11.4	2.5	0.5	–	–	50.7	0.88	25.1	0.77	1.41	1.02
	Series 9-71	PO	M	1	20.0	4.5	5	0.063	13.9	11.4	2.5	0.5	–	–	50.7	0.76	20.3	0.64	1.14	0.83
	Series 9-72	PO	M	1	20.0	4.5	5	0.069	13.9	11.4	2.5	0.5	–	–	50.7	0.89	23.1	0.78	1.30	0.94
	Series 18-135	PO	C	1	40.0	4.5	5	0.072					–	–	30.1	2.53	17.2	0.00	1.25	1.21
	Series 18-136	PO	C	1	40.0	4.5	5	0.072					–	–	30.1	2.00	16.1	0.00	1.17	1.14
Prince et al. (2014)[65]	A8R0	PO	C	3	8.0	5.8	5	0.085	5.9	5.4	1.2		–	–	34.0	0.71	23.3	1.33	1.60	1.14
	A10R0	PO	C	3	10.0	4.5	5	0.093	7.5	6.8	1.2		–	–	34.0	0.58	18.0	0.90	1.23	0.91
Huang et al. (2016)[66]	S000-P000-II-C	PO	C	1	20.0	3.3	3	0.096	10.4	8.4	2.0	1.0	6	4	38.0	0.78	18.0	0.80	1.16	0.93
Koschemann et al. (2022)[22]	C40-PO	PO	C	3	16.0	5.8	2	0.065	9.6	5.6	4.0	1.1	–	–	49.2	0.74	21.4	1.00	1.22	0.86
	C40-BE-4	BE	C	3	16.0	4.0	2	0.065	9.6	5.6	4.0	1.1	6	2	49.2	0.79	26.1	1.06	1.49	1.05
	C40-BE-3	BE	C	3	16.0	3.0	2	0.065	9.6	5.6	4.0	1.1	6	2	49.2	0.65	26.1	0.88	1.49	1.05
	C80-P	PO	C	6	16.0	5.8	2	0.065	9.6	5.6	4.0	1.1	–	–	95.6	0.71	41.5	1.19	1.70	0.96
	C80-BE-4	BE	C	3	16.0	4.0	2	0.065	9.6	5.6	4.0	1.1	6	2	95.6	0.28	40.6	0.47	1.66	0.94
	C80-BE-3	BE	C	3	16.0	3.0	2	0.065	9.6	5.6	4.0	1.1	6	2	95.6	0.26	39.6	0.44	1.62	0.92
	C120-PO	PO	C	6	16.0	5.8	2	0.065	9.6	5.6	4.0	1.1	–	–	119.7	0.96	52.1	1.74	1.90	1.00
	C120-BE-4	BE	C	3	16.0	4.0	2	0.065	9.6	5.6	4.0	1.1	6	2	119.7	0.60	50.2	1.09	1.84	0.96
	C120-BE-3	BE	C	7	16.0	3.0	2	0.065	9.6	5.6	4.0	1.1	6	2	119.7	0.46	50.3	0.83	1.84	0.97
All tests																	Avg[a]	1.00	1.31	1.00
																	CoV[a]	26%	23%	11%

Abbreviations: BE, beam-end test; C, commercial; M, machined; MPO, modified pull-out test; PO, pull-out test.

[a]Average value and coefficient of variation calculated without weighted values on the basis of multiple specimens.